Reviews

Synthesis and Enhanced Intercalation Properties of Nanostructured Vanadium Oxides

Ying Wang and Guozhong Cao*

Department of Materials Science and Engineering, University of Washington, Seattle, Washington 98195

Received December 14, 2005. Revised Manuscript Received February 15, 2006

Nanomaterials lie at the heart of the fundamental advances in efficient energy storage/conversion and other types of nanodevices in which the surface process and transport kinetics play determining roles. This review describes some recent developments in the synthesis and characterizations of various vanadium oxide nanostructures including nanowires, nanorolls, nanobelts, and ordered arrays of nanorods, nanotubes, and nanocables for significantly enhanced intercalation properties. The major topic of this article is to highlight the lithium ion intercalation properties of nanostructured vanadium oxides for energy storage as well as other applications in sensors, actuators, and transistors.

1. Introduction

The technological limits of present microdevices have stimulated wide research activities targeted at downsizing the devices by at least an order of magnitude, and nanomaterials are the perfect building blocks for this purpose. The reduction in the necessary amount of functional materials leads to reduction of toxicity and less use of resources. Most importantly, nanomaterials offer the unusual mechanical, electrical, and optical properties endowed by confining the dimensions of such materials, and the overall behavior of nanomaterials exhibits combinations of bulk and surface properties.[1] Thus, nanostructured materials are drawing a tremendous amount of attention because of their novel properties and because of their potential applications in various nanodevices, such as field-effect transistors (FETs)[2−5] chemical and biological sensors,[6−9] nanoprobes,[10] and nanocables.[11] Furthermore, the emerging energy resource crisis and ecological concerns unambiguously show that energy storage is one of the great challenges in the current century. It is critical that low-cost, lightweight, small-volume, and environment friendly energy storage/conversion devices are developed, and nanomaterials are attracting great interest for electrochemical energy storage, for example, the rechargeable lithium ion batteries. The reports on the processing, properties, and applications of nanomaterials are rapidly appearing on a daily basis. The purpose of the present work is to give an in-depth survey of recent progress on synthesis and characterizations of nanomaterials by choosing vanadium pentoxide (V_2O_5) as a model material system. As a result of the multiple valence state of vanadium, vanadium pentoxide has versatile redox-dependent properties and finds wide applications in catalysis,[12] electrochromism,[13−15] and electrochemistry.[16−18] The nanostructured form of this material has been employed in FETs,[19] sensors,[20,21] spintronic devices,[22] and nanolithography templates.[23,24]

Vanadium pentoxide is a typical intercalation compound as a result of its layered structure. Intercalation compounds are a special family of materials. The intercalation refers to the reversible intercalation of mobile guest species (atoms, molecules, or ions) into a crystalline host lattice that contains an interconnected system of an empty lattice site of appropriate size, while the structural integrity of the host lattice is formally conserved.[25] The intercalation reactions typically occur around room temperature. A variety of host lattice structures have been found to undergo such low-temperature reactions.[26] However, the intercalation reactions involving layered host lattices have been most extensively studied, partly because of the structural flexibility and the ability to adapt to the geometry of the intercalated guest species by free adjustment of the interlayer separation. The readers are referred to a comprehensive and excellent article on inorganic intercalation compounds.[25] Despite the differences in chemical composition and lattice structure of the host sheets, all the layer hosts are characterized by strong interlayer covalent bonding and weak interlayer intercalations. The weak interlayer intercalations include van der Waals force or electrostatic attraction through oppositely charged species between two layers. Various host lattices are metal dichalcogenides, metal oxyhalides, metal phosphorus trisulfides, metal oxides, metal phosphates, hydrogen phosphates, phosphonates, and graphite and layered clay minerals. Guest materials include metal ions, organic molecules, and organometallic molecules. When guest species are incorporated into host lattices, various structural changes will take place. The principle geometrical transitions of layered host lattice matrixes upon intercalation

* To whom correspondence should be addressed. E-mail: gzcao@u.washington.edu. Tel.: 206-616-9084. Fax: 206-543-3100.

10.1021/cm052765h CCC: $33.50
Published on Web 05/12/2006

of guest species include (1) change in interlayer spacing, (2) change in stacking mode of the layers, and (3) formation of intermediate phases at low guest concentrations that may exhibit staging.[27] There are various synthesis methods for the formation of intercalation compounds.[25,28] The most commonly used and simplest method is the direct reaction of the guest species with the host lattice.[29] For direction reactions, the intercalation reagents must be good reducing agents of the host crystals. Ion exchange is a method to replace the guest ion in an intercalation compound with another guest ion, which offers a useful route for intercalating large ions that do not directly intercalate.[30] Appropriate chosen solvents or electrolytes may assist the ion exchange reactions by flocculating and reflocculating the host structure.[31] Electrointercalation is yet another method, in which the host lattice serves as the cathode of an electrochemical cell.[32] Electrochemical lithium intercalation occurs together with compensating electrons leading to the formation of vanadium bronzes as follows:

$$V_2O_5 + xLi^+ + xe^- \leftrightarrow Li_xV_2O_5 \quad (1)$$

Whittingham et al. have presented comprehensive reviews on lithium battery cathode materials including lithium metal oxides and vanadium oxides.[33,34] For Li-ion intercalation applications, vanadium pentoxide offers the essential advantages of low cost, abundant source, easy synthesis, and high energy densities.

In addition to crystalline V_2O_5, rather promising results have been reported for hydrated vanadium pentoxide ($V_2O_5 \cdot nH_2O$), such as $V_2O_5 \cdot nH_2O$ glasses with P_2O_5 or other network formers,[35] $V_2O_5 \cdot nH_2O$ xerogels,[36,37] and $V_2O_5 \cdot nH_2O$ aerogels.[38] Specific energies of over 700 W·h/kg were measured for lithium cells with a xerogel positive electrode.[37] $V_2O_5 \cdot nH_2O$ xerogels are composed of ribbonlike particles and display lamellar ordering, with water molecules intercalated between the layers.[39] These water molecules expand the distance between the layers, and the intercalation capacities of $V_2O_5 \cdot nH_2O$ xerogels are enhanced as a result.[37] However, the intercalation capacity and charge/discharge rate of V_2O_5 are limited by the moderate electrical conductivity ($10^{-2}-10^{-3}$ S/cm)[20,40] of V_2O_5 and the low diffusion coefficient of Li ions ($10^{-12}-10^{-13}$ cm^2/s)[41,42] in the V_2O_5 matrix. Many studies have been conducted to improve lithium diffusion and electrical conduction performance in V_2O_5 by crystal structure modification toward a more open structure[43] and by coating of V_2O_5 on highly conductive materials.[44] Other approaches include making use of nanostructured materials that possess large surface area and short diffusion paths.

In this paper, the aspect of nanostructured vanadium pentoxide used in electrochemical energy storage will be addressed in detail, whereas we will also touch on the utilization of nanostructured V_2O_5 in other nanodevices such as sensors, actuators, and transistors. Selected recent examples from our laboratory and other research groups illustrate the synthesis and characterizations of a large variety of one-dimensional nanostructured V_2O_5, including nanowires[45−48] nanobelts,[21] nanorolls,[49] ordered arrays of nanorods,[50−52] nanotubes,[53] and nanocables.[54] It is the uncomplicated sol−gel processing (soft chemistry) method in combination with template synthesis or hydrothermal treatment that produces the most desirable nanostructures with remarkable reliability, efficiency, selectivity, and variety. Further, without any external effort, negatively charged nanowires of vanadium pentoxide can grow spontaneously in the sol. Other fabrication methods of vanadium pentoxide nanostructures include the reverse micelle technique, and the size of the nanorods of V_2O_5 can be tuned easily by keeping the freshly made nanorods in the micellar solution.[55] Whittingham's group recently reported another new method to produce vanadium oxide nanofibers with dimensions less than 140 nm by coating vanadium oxide on polylactide fibers.[56] Electrochemical studies reveal that these vanadium oxide nanofibers are redox active and readily undergo reversible reactions with lithium ions.

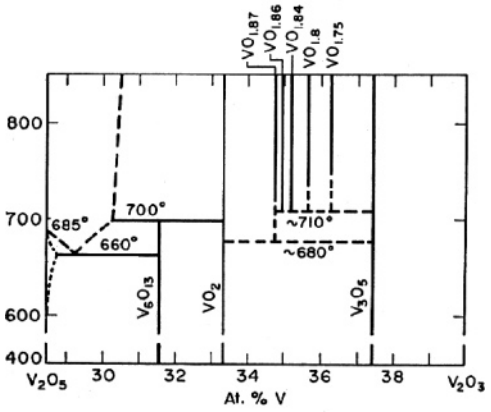

Figure 1. Partial phase diagram of the vanadium−oxygen binary system showing a variety of vanadium oxides stable at low temperatures with vanadium having valence states varying between +3 and +5 and more metastable vanadium oxides formed at higher temperatures. (Reprinted with permission from ref 57. Copyright 1957 Societe Chimica Italiana.)

2. Structures and Properties of Vanadium Oxides

Like most transitional metals, vanadium can exist in different valence states and consequently form a variety of oxides including VO, V_2O_3, VO_2, and V_2O_5. Figure 1 presents the partial phase diagram of the V−O binary system.[57] In addition to these simple oxides, there are many other closely related structures where vanadium atoms have different valences between V_2O_3 (+3) and VO_2 (+4) and between VO_2 (+4) and V_2O_5 (+5). The series V_nO_{2n-1} ($1 < n < 9$) between VO_2 and VO_3, as well as V_2O_5, V_4O_9, V_6O_{13}, and V_3O_7 have all been observed.[58] Hence, the phase equilibria in the vanadium−oxygen system are rather complicated.[59] Vanadium oxides display a complex structural chemistry. For example, VO_2 exhibits a rutile structure[60] while $VO_2 \cdot 0.5H_2O$ has a layer structure.[61] The structure of V_2O_5 exhibits characteristic features of two-dimensional vanadium oxides.[62] Mixed valence materials of V (+4)/V (+5) show a particularly rich crystal chemistry. The detailed and useful structural classification of various vanadium oxides can be found in a review by Zavalij and Whittingham.[63] Among vanadium oxides, only V_2O_5 and V_6O_{13} have gained importance as intercalation materials.

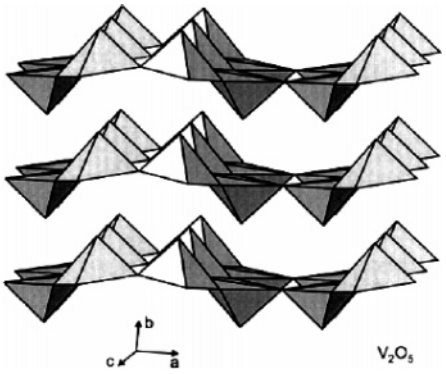

Figure 2. Crystal structure of V_2O_5 consisting of layers of VO_5 square pyramids that share edges and corners with the apical V−O bond distance being much shorter than the four other distances and corresponding to a double bond. (Reprinted with permission from ref 66. Copyright 1998 Wiley-VCH.)

Orthorhombic crystalline V_2O_5 consists of layers of VO_5 square pyramids that share edges and corners.[64,65] Figure 2 presents the crystal structure of V_2O_5.[66] The apical V−O bond distance is much shorter than the four other distances and corresponds to a double bond. The layered structure of V_2O_5 illustrates a two-dimensional character for this material; however, the structure of V_2O_5 can be described as distorted VO_6 octahedral as well.[67,68] The structural anisotropy of this material is illustrated by the very large length of the sixth V−O bond which gives rise to the ability to insert guest species in perovskite-like cavities.

Low-crystalline hydrated vanadium pentoxide ($V_2O_5 \cdot nH_2O$) is another Li-ion intercalation material, but its crystal structure has not been solved until recently. Petkov et al. have recently determined the full three-dimensional structure of $V_2O_5 \cdot nH_2O$ using the atomic pair distribution function (PDF) technique,[69] which is particularly powerful for structural characterization of crystalline materials with significant intrinsic disorder.[70] This technique takes both the Bragg as well as the diffuse component of the diffraction data into account and thus yields structure parameters reflecting both the long-range order and the local structural disorder in materials. The structure of the $V_2O_5 \cdot nH_2O$ xerogel can be illustrated as an assembly of well-defined bilayers of single V_2O_5 layers made of square pyramidal VO_5 units with water molecules residing between them. This structure possesses enough atomic ordering perhaps to be characterized as nanocrystalline. As summarized earlier, crystalline V_2O_5 is an ordered assembly of single layers of V_2O_5. The $V_2O_5 \cdot nH_2O$ xerogel is a stack of long ribbonlike slabs which are bilayers of single V_2O_5 layers made up of square pyramidal VO_5 units, as shown in Figure 3a. The closest distance between the bilayers is about 11.5 Å. When the xerogel intercalates or extracts guest species, this distance expands or contracts correspondingly. The distance between the two single sheets of V_2O_5 making up the bilayer slab is approximately 2.90 Å. The coordination environment of V atoms in each bilayered slab can be taken as octahedral. The VO_5 octahedra share edges to from double chains propagating down the *b* axis. These double chains then arrange in parallel and side by side via interchain V−O bonds by sharing corners of octahedra to form the slab. Similarly, crystalline V_2O_5 consists of monolayered slabs composed of parallel double chains. on the basis of such one-dimensional chain-based slab structure, needlelike crystal growth appears in crystalline V_2O_5 and long nanoribbons are formed in the $V_2O_5 \cdot nH_2O$ xerogel. Figure 3b shows the thermogravimetric trace for $V_2O_5 \cdot nH_2O$ xerogels.[71] It reveals the existence of 1.6 mol of water per mole of oxide at room temperature (assuming V_2O_5 as the solid phase after heating at >330 °C, whereas water is the only volatile phase in the initial film). The weight change profile for the xerogel is characterized by a steep loss between room temperature and 100 °C, followed by a more gradual weight loss up until 330 °C. Thermal treatment at 110 °C produced a xerogel with the $V_2O_5 \cdot 0.6H_2O$ composition. Continued heating to 250 °C produced $V_2O_5 \cdot 0.3H_2O$ by removing bound water. Heating above 300 °C induced loss of tightly bound water and crystallization of material, as discussed in the X-ray diffraction (XRD) results. For $V_2O_5 \cdot nH_2O$, the interlayer spacing *d* can be calculated from the diffraction angle of the (001) peak.[1,72] Figure 3c summarizes the dependences of interlayer spacing on the *n* value in $V_2O_5 \cdot nH_2O$.[71] For samples treated at 25, 110, and 250 °C, the interlayer spacings show a slight decrease from 11.74 to 11.15 Å as the temperature goes higher; however, the change is rather small and the results are consistent with the 11.5 Å reported in previous reports.[39] For the sample annealed at 300 °C in which low-crystalline $V_2O_5 \cdot nH_2O$ coexists with orthorhombic V_2O_5, the interlayer spacing of $V_2O_5 \cdot nH_2O$ is 8.43 Å, apparently smaller than the samples treated from 25 to 250 °C. Thermogravimetric analysis (TGA) results have shown that 110 °C corresponds to $V_2O_5 \cdot 0.6H_2O$ and 250 °C corresponds to $V_2O_5 \cdot 0.3H_2O$. It can be concluded that interlayer spacings do not change much when only bound water (reversibly absorbed or hydrogen-bonded water) is removed. These parameters will alter considerably only when tightly bound (chemically bonded) water is removed and the material is on the verge of crystallization.

Vanadium pentoxide can intercalate a large variety of molecules and ions. The intercalation of organic molecules by V_2O_5 can be found in a review by Hagrman et al.[73] The Ag or Cu doped vanadium pentoxide xerogels can function as high capacity (500−500 mA·h/g) and high-energy cathode materials in lithium batteries.[74] Vanadium oxides that contain Ag or Cu are particularly interesting because Ag or Cu ions can be exuded from the lattice increasing the electronic conductivity of the cathode material. The compound $Ag_2V_4O_{11}$ has been commercially used as the cathode material for the power source in medical devices.[75] Another compound $Cu_{2.33}V_4O_{11}$ has attracted much attention and has been reported to be more rechargeable than the silver vanadium oxide.[76] Electro-oxidation of $Cu_{2.33}V_4O_{11}$ yields a new compound $Cu_{1.1}V_4O_{11}$ which exhibits enhanced cycling performance with a capacity of about 200 mA·h/g at the current densities from 0.1 to 1 mA/cm^2 over the first 20 cycles.[77]

The reversible electrochemical lithium intercalation into V_2O_5 at room temperature was first reported by Whittingham in 1975.[78] Afterward several phases were observed depending on the amount of inserted lithium: α and ϵ phases exist for $x < 0.01$ and $0.35 < x < 0.7$ in $Li_xV_2O_5$, respectively,

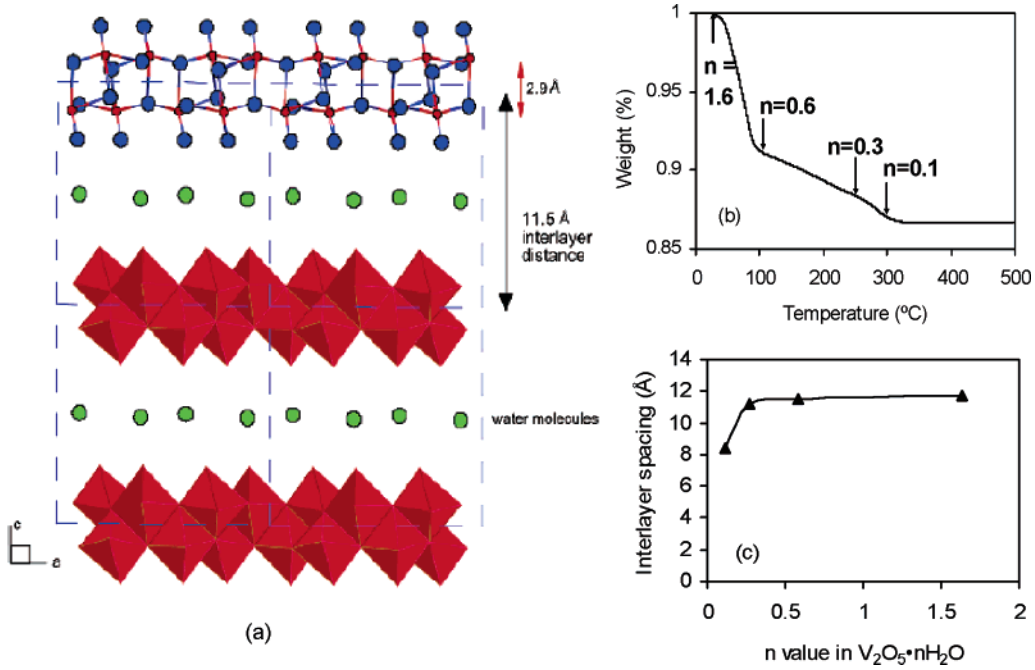

Figure 3. (a) Structure of the $V_2O_5 \cdot H_2O$ xerogel (polyhedra and ball-stick model) as revealed by PDF analysis. Characteristic distances are shown. Water molecules are round dots between the layers. (Reprinted with permission from ref 69. Copyright 2002 American Chemical Society.) (b) TGA curve for $V_2O_5 \cdot nH_2O$ xerogels. (c) Dependence of interlayer spacing on the n value in $V_2O_5 \cdot nH_2O$. (Reprinted with permission from ref 71. Copyright 2005 American Chemical Society.)

showing a V_2O_5-type structure with increasing puckering of the layers.[79] The composition LiV_2O_5 corresponds to the δ phase formed by gliding of one layer out of two.[80] For $x \leq 1$, the original V_2O_5 structure can be recovered upon lithium deintercalation and the phase transitions are fully reversible.[81] However, for further lithium intercalation ($x > 1$), a reconstruction mechanism leads to the irreversible transformation from the δ phase the γ-phase.[79] This γ-phase can be reversibly cycled in the stoichiometric range $0 < x < 2$ without changing the γ-type structure.[82,83] Upon further intercalation of a third lithium, the γ-phase will be irreversibly transformed to the ω-phase with a rock-salt type structure. This ω-phase can be prepared either electrochemically at a potential of about 1.2 V versus Li/Li^+ or chemically using an excess of butyllithium.[84,85] Almost all the lithium from the ω-phase can be electrochemically deintercalated again. The resulted compound demonstrated a specific energy of up to 900 W·h/kg and 100 cycles with more than 450 W·h/kg cell in a voltage range between 3.4 and 1.9 V and thus showed great potential as a positive electrode material for secondary lithium batteries, which has been demonstrated for a ω-$Li_xV_2O_5$/Li.[86] Figure 4 presents the evolution of $Li_xV_2O_5$ phases as lithium is intercalated into V_2O_5 and the cycling of the ω-phase.[87] Hydrated vanadium pentoxide ($V_2O_5 \cdot nH_2O$) has also been widely studied for lithium ion applications. These low-crystalline materials have morphologies significantly different from those of crystalline V_2O_5 and offer essential advantages of a large electrochemically active surface area, small particle size, and low density. These characteristics provide both high overall diffusion coefficients and low volume expansion during lithium intercalation. However, limited long-term cycling stability is a major challenge of such electrode materials at present. Zakharova and Volkov[88] and Dong et al.[89] have summarized the Li-ion intercalation properties of $V_2O_5 \cdot nH_2O$ xerogels and aerogels, respectively.

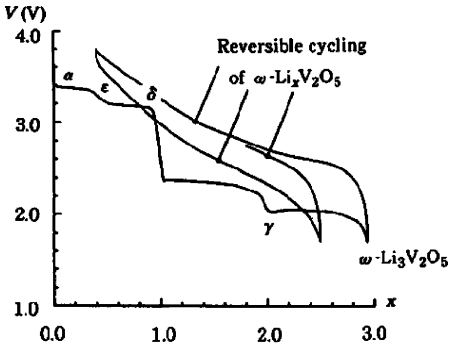

Figure 4. Evolution of $Li_xV_2O_5$ phases with degree of lithium intercalation into V_2O_5 and the cycling of the ω-phase. The α-, ϵ-, δ-, γ-, and ω-phases correspond to $x < 0.01$, $0.35 < x < 0.7$, $x = 1$, $1 < x < 3$, and $x = 3$, respectively. x is moles of lithium intercalated per mole of V_2O_5. The ω-phase cycles in a single solid-solution phase with the last lithium coming out at over 4 V and shows the difference between this phase and the initial vanadium pentoxide phase, which has an open circuit voltage of 3.5 V. (Reprinted with permission from ref 87. Copyright 1994 Elsevier.)

3. Synthesis of Vanadium Oxide Nanostructures

Vanadium pentoxide gels can be easily synthesized from both inorganic and metal−organic precursors and remain stable for years. Sol−gel processing is the major method that has been used to prepare this gel. Many synthesis methods of vanadium pentoxide sols or gels have already been described in the literature. Ditte reported the first one in 1885 by heating ammonium vanadate in a platinum crucible, followed by reaction with hot nitric acid and mixing into water, which produced a red sol.[90] A similar synthetic procedure by using hydrochloric acid was reported later.[91] Aqueous solutions of $VOCl_3$ were later discovered to yield V_2O_5 sols through the thermohydrolysis.[92] The alcoholic sol−

gel routes employing hydrolysis and condensation of vanadium alkoxides $VO(OR)_3$ (R = alkyl chain**)** have been used since the beginning of the century. In addition to organic precursors, inorganic oxides can directly produce vanadium pentoxide gels as well. For example, a red aqueous sol of vanadium pentoxide can be achieved by reacting hydrogen peroxide with crystalline V_2O_5 powders.[93] Even more simply, vanadium pentoxide gels can be obtained by melting the oxide heated around 800 °C followed by pouring into water,[94] which facilitates large-scale production in industry. Moreover, vanadium pentoxide gels were found to be formed from hydration of amorphous V_2O_5.[95] The amorphous oxide was obtained by splat-cooling from the melt, vapor deposition,[96] or O_2-H_2 flame fusion. Gels or colloidal solutions are resulted from dissolving these oxides into water. This hydration process was described as the swelling of a polymeric network into the solvent. Hydration seems to be characteristic of the amorphous state.

Recent sol−gel syntheses of vanadium pentoxide gels are grouped into three convenient routes: (1) acidification of $NaVO_3$ using an ion-exchange process and polymerization of the resultant HVO_3 in water,[97,98] (2) hydrolysis and condensation of vanadium alkoxide,[99,100] and (3) reaction between H_2O_2 and V_2O_5 powder.[101,102] Synthesis of V_2O_5 has been dominated by the $NaVO_3$ route, and detailed research has been done on both the $NaVO_3$ route and the V alkoxide route to investigate the reaction mechanisms. For exmple, Holland et al. have recently compared thermal behavior and Li^+ diffusion constants in $V_2O_5{\cdot}nH_2O$ xerogels prepared from the $NaVO_3$ and V alkoxide routes.[103] Their report revealed that the $V_2O_5{\cdot}nH_2O$ xerogels made from these two methods have significant differences besides many similarities. Although the $NaVO_3$ route is the most commonly used and the V alkoxide route has been used increasingly, these two methods suffer from a few disadvantages. The $NaVO_3$ route may introduce contamination of sodium ions, and the concentration of vanadium is subject to change because of the additional water in the resin during the ion-exchange process. The ion-exchange process also causes a difficulty for large-scale production. In the V alkoxide route, the high reactivity of the alkoxide and its dependence on pH, temperature, and reactant concentrations make the chemical synthesis of $V_2O_5{\cdot}nH_2O$ gels rather delicate and difficult. A complexing agent such as acetic acid or acetyl acetone can be added to control the reaction rate; however, these agents also introduces complicated chemistry and the resultant sol may undergo slow side reactions for a long time. Therefore, the simple and clean $H_2O_2-V_2O_5$ route has attracted more and more attention recently. This method excludes the presence of foreign ions or organic ligands and offers precise control of vanadium concentration. The synthetic pathway and gelation process of the $H_2O_2-V_2O_5$ route have been studied by ^{51}V NMR and laser Raman spectroscopic techniques lately.[102] Our group has specifically utilized this method to obtain a stable $V_2O_5{\cdot}nH_2O$ sol which can be used in various deposition processes including electrophoretic deposition. Comprehensive reviews on synthesis and properties of vanadium pentoxide gels can be referred to Livage's two articles.[20,97] The orthorhombic phase of crystalline V_2O_5 is usually obtained by heating vanadium pentoxide gels above 350 °C in air.

This section reviews the major methods, that is, template synthesis and hydrothermal synthesis, that have been used to synthesize the various nanostructures of vanadium oxides in the present paper. Among many methods for the fabrication of nanomaterials ranging from physical techniques to chemical methods,[104,105] template synthesis is one of the most important methods for synthesizing one-dimensional nanostructures. This process involves synthesizing a desired material within the pores of a porous membrane. A nanocylinder of the desired material is obtained in each pore because the membranes that are used have cylindrical pores of uniform diameter. The nanocylinder can be solid to yield a nanorod or hollow to yield a nanotube, depending on the properties of the material and the chemistry of the pore wall. Template membranes are track-etched polycarbonate (PC) membranes and anodic alumina membranes sold by a number of companies such as Millipore. The most straightforward and versatile template synthesis of nanostructures is template filling. Either a melt or a liquid precursor can be used to fill the pores. There are several concerns in the template filling. First, the wetability of the pore wall should be good enough to permit the penetration and complete filling of the liquid precursor or precursor mixture. For filling at low temperatures, the surface of pore walls can be easily modified to be either hydrophilic or hydrophobic by introducing a monolayer of organic molecules. Second, the template materials should be chemically inert. Third, control of shrinkage during solidification is required. If adhesion between the pore walls and the filling material is weak or solidification starts at the center, from one end of the pore, or uniformly, solid nanorods are most likely to form. However, if the adhesion is very strong or the solidification starts at the interfaces and proceeds inwardly, it is most likely to form hollow nanotubes. Electrochemical deposition is also called electrodeposition, a process involving electrochemical reaction that results in the deposition of solid material on an electrode. Nanocomposites are produced when the deposition is confined inside the pores of template membranes. Nanorods or nanotubes subsequently result when the template membrane is removed. During the electrodeposition, the electrode is separated from the depositing solution by the deposit after the initial deposition, and the electrical current must go through the deposit to allow the deposition process to continue. Therefore, electrochemical deposition is only applicable to electrical conductive materials such as metals, alloys, semiconductors, and electrical conductive polymers. Thus, the nanomaterials produced by template electrodeposition are mostly metals, chalcogenide semiconductors, and conducting polymers. Rarely can oxides be synthesized by this process, although a few semiconducting oxide nanostructures have been formed through conventional or novel electrochemical processes. The template-based electrodeposition process starts with coating one face of the membrane with a thin noble metal film via either ion sputtering or thermal evaporation. Thus, the coated membrane is then used as an electrode for electroplating. A general review on template synthesis can be found in Hulteen and Martin's article.[106] Finally, the template method can be

combined with electrophoretic deposition. The major difference between electrophoretic deposition and electrochemical deposition is that the material deposited by electrophoretic deposition need not be electrically conductive. Electrophoretic deposition simply uses such an oriented motion of charged particles to grow films or monoliths by enriching the solid particles from a colloidal dispersion or a sol onto the surface of an electrode. At the beginning of the nanostructure growth, charged sol particles move as a result of electrophoresis toward the negative electrode. They deposit at the bottom of the pore, while the oppositely charged counterions move in the opposite direction. As time increases, the densely packed sol particles fill more of the pore, until the pore is completely filled. Fundamentals and practical approaches in growing oxide nanorod arrays through sol−gel processing and template-based electrophoretic deposition can be found in our published feature article.[107]

Hydrothermal synthesis is another powerful processes employed in nanochemistry. Especially when exposed to supercritical conditions, many starting materials undergo quite unexpected reactions that are often accompanied by the formation of nanoscopic morphologies, which are not accessible by classical routes. Another benefit from hydrothermal synthesis is the wide variety of parameters that can be chosen and combined: reaction temperatures close to room temperature or above 100 °C, variations in the pH value of the systems, concentration of solvents, introduction and removal of templates and other additives, choice of different autoclave geometries, and so forth.[108] Combinatorial methods might be a suitable approach toward systematization of these parameter fields, but the problem of subsequent scale-up procedures always remains to be solved after a breakthrough in hydrothermal combinatorial synthesis. If, however, a standard procedure for hydrothermal formation of nanoparticles has been established, then these hydrothermal reactions are outstandingly efficient (almost 100% conversion of the starting material), time-saving, and experimentally effortless, such as the low-cost synthesis of vanadium oxide nanotubes.[109] When planning a hydrothermal synthesis of nanostructures with a distinct anisotropic morphology, it is always convenient to start from an educt with a layered structure, especially when a template is involved.

4. Nanostructures of Vanadium Oxides with Enhanced Intercalation Properties

4.1. Nanorod Arrays of Polycrystalline Vanadium Oxide. Patrissi and Martin have used the template synthesis method to prepare nanostructured electrodes of orthorhombic V_2O_5 and have studied the effects of Li-ion diffusion distance and surface area on V_2O_5 rate capability.[114] Nanorod arrays of polycrystalline V_2O_5 were prepared by depositing triisopropoxyvanadium(V) oxide (TIVO) into the pores of microporous PC filtration membranes. TIVO then underwent hydrolysis in the glovebox and condensation in an oxygen atmosphere, followed by sintering at 400 °C. The resultant sample is an ordered array of V_2O_5 which protruded from a V_2O_5 surface layer like the bristles of a brush. Figure 5 shows such nanorod arrays with various diameters and the PC filtration membranes. For nanorods that have the diameter

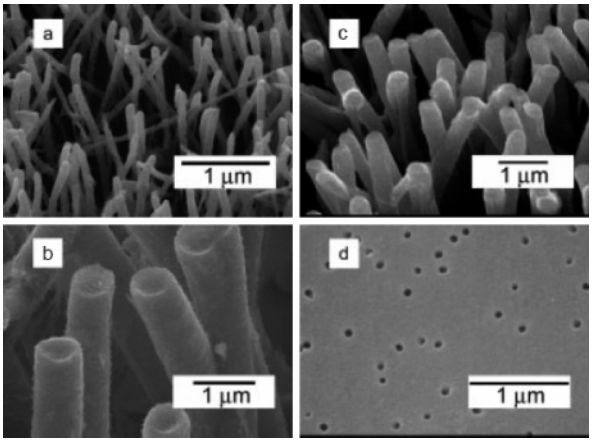

Figure 5. SEM images of (a) the 70-nm-diameter V_2O_5 nanorod array, (b) the 0.8-μm-diameter V_2O_5 nanorod array, (c) the 0.45-μm-diameter V_2O_5 nanorod array, and (d) the PC template used to prepare the 70-nm-diameter nanorod array. (Reprinted with permission from ref 119. Copyright 2005 Wiley-VCH.)

of 115 nm and the length of 2 mm, the galvanostatic discharge performance of such nanostructured V_2O_5 electrodes was compared to a thin-film electrode of similar V_2O_5 mass and geometric area. Although the Li^+ storage capacity of the thin-film electrode was equivalent to that of the nanostructured electrode at low (C/20) discharge rates, the nanostructured electrode demonstrated higher capacity than the film electrode at the high discharge rate. For example, the nanostructured electrode delivered three times the capacity of the thin film electrode at a rate of 200C; above 500C the nanostructured electrode delivered four times the capacity of the thin-film control electrode.

There have been intensive studies on applying nanotechnology into Li-ion battery design, and most of them are focused on the room-temperature performance.[110−114] Li-ion batteries are efficient, lightweight, and rechargeable power sources for consumer electronics. However, the poor low-tempeature performance of Li-ion batteries precludes the utilization of these batteries in a number of defense, space, and terrestrial applications.[115] The amount of charge delivered from the battery at temperatures below 0 °C is substantially lower than the amount of charge delivered at room temperature.[116−118] Li-ion battery electrodes composed of nanosized material may counter this low-temperature performance challenge, because nanomaterials can palliate the slow electrochemical kinetics problem and the slow diffusion problem by offering high surface area and short diffusion distance. Sides and Martin have demonstrated this case by showing that nanorods (diameter = 70 nm) of the electrode material V_2O_5 deliver dramatically higher specific discharge capacities at low temperature than V_2O_5 rods with micrometer-sized diameters.[119] The template synthesis method was used to prepare cathodes composed of V_2O_5 nanorods or microrods with various diameters: 70 nm, 0.8 μm, and 0.45 μm as shown in Figure 5. The charge/discharge reactions and performance of these electrode materials were then investigated at different temperatures: 25, 0, and −20 °C. The emplate method allows the surface area of the electrode to be calculated from the fiber diameter, length, and pore density of the template membrane. The calculations show that 0.45 μm has the highest surface area, and the 0.8 μm

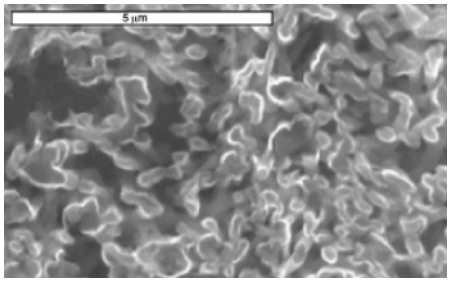

Figure 6. SEM image (top view) of template-synthesized the V_2O_5 nanorod array obtained from the etched PC membrane. The pore diameter of the PC membrane is 50 nm prior to etching. (Reprinted with permission from ref 126. Copyright 2001 Electrochemical Society.)

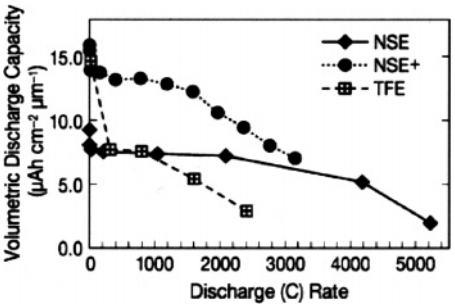

Figure 7. Comparison of volumetric capacity as a function of discharge rate for three types of V_2O_5 electrodes. NSE is the nanorod array obtained from the etched 50-nm-diameter PC template; NSE+ is the nanorod array prepared from the etched 50-nm-diameter PC template followed by applying additional sol−gel precursor; and TFE is the thin-film control electrode. (Reprinted with permission from ref 126. Copyright 2001 Electrochemical Society.)

electrode has the lowest; the surface area of the 70 nm electrode is in between. However, it was found 70-nm-diameter nanorod arrays had the best low-temperature performance among the three, and the result is ascribed to its nanoscale (below 100 nm) and short diffusion distance. The poor low-temperature performance of Li-ion batteries is either due to a decrease in the diffusion coefficient within the electrode particles or due to a decrease in the rate of the electrode reactions with decreasing temperature. The experimental results of the 70 nm electrode having the best low-temperature performance show that temperature dependence of the solid-state diffusion coefficient determines the low-temperature performance of the electrodes.

For a large variety of Li-ion battery electrode materials, significant improvements in rate capabilities have been observed for the template-prepared nanostructured electrodes.[120−132] Furthermore, a high volumetric energy density for the electrode is desired, because reduction in the size of consumer electronic devices has made the size reduction of Li-ion batteries necessary. PC membranes and alumina membranes are the two templates commonly used in preparing nanostructured electrodes. Alumina membranes have much higher porosity than PC membranes. However, removal of alumina membranes is accomplished by dissolving the membranes in acidic or basic solutions. Unfortunately, most electrode materials are oxides that are also soluble in these solutions, and the nanorod arrays will be dissolved along with the alumina templates. Therefore, a PC template is the remaining choice. The porosities of the PC membranes are rather low, for example, 1.2% for membranes that have 50-nm-diameter pores. Accordingly, this low porosity limits the number of nanorods of the electrode material and the resultant volumetric energy density of the nanostructured electrode.

Li and Martin have recently achieved improved volumetric energy densities of nanostructured electrode materials by chemically etching the PC membrane to increase its porosity prior to template synthesis.[124] Figure 6 shows the scanning electron microscopy (SEM) image (top view) of the nanostructured V_2O_5 cathodes prepared from such an etched PC template.[126] The pore diameter prior to etching is 50 nm. Such a nanostructured electrode is denoted as NSE. Furthermore, for some nanostructured electrodes obtained from etched templates, additional sol−gel precursor material was applied to the surfaces after template synthesis and removal of the etched membrane to further enhance the volumetric energy density. The resultant electrode is labeled as NSE+. The rate capabilities of the NSE and NSE+ are compared to that of the thin film control electrode (shorted as TFE). Figure 7 summarizes the volumetric discharge capacities of these three typical electrodes as a function of discharge rate. At high discharge rate, both NSE+ and NSE electrodes have higher volumetric capacity than the TFE electrode, and NSE+ has the highest. At a lower discharge rate, the NSE+ electrode still has higher volumetric capacity than the TFE electrode. These results unambiguously demonstrate that template synthesis can be utilized to prepare nanostructured electrodes with good rate performance and high volumetric energy densities.

Table 1. Growth Condition and Shrinkage of Vanadium Pentoxide Nanorod Arrays from These Three Different Routes

	route	vanadium species	growth electrode	shrinkage after firing
A	valence change	VO^{2+} ion	(+)	0%
B	pH change	VO_2^+	(−)	15%
C	sol−gel	colloid	(+)	50%

4.2. Nanorod Arrays of Single-Crystalline Vanadium Oxide. The advantage of template-based growth methods is the ability of fabricating unidirectionally aligned and uniformly sized nanorod arrays of a variety of materials. However, such methods suffer from inherent limitations. In particular, nanorods or nanowires synthesized by template-based growth methods are commonly either amorphous or polycrystalline and porous, which limits further studies on microstructure, properties and applications of such grown nanorods or nanowires. In addition, postdeposition annealing at elevated temperatures is often required to achieve desired density and mechanical integrity. Poor mechanical integrity and postdeposition annealing often result in break, distortion, and agglomeration of grown nanorods. Further study and development of template-based growth of single-crystal nanorods are obviously of significant importance; however, very limited research has been reported in the literature so far.

Single-crystal vanadium pentoxide nanorod arrays have been grown inside PC templates with the assistance of electric field from three different types of solutions or sol. Table 1 summarizes the growth conditions and shrinkage of V_2O_5 nanorod arrays grown from three different solutions or sols, that is, VO^{2+} solution (route A), VO_2^+ solution (route

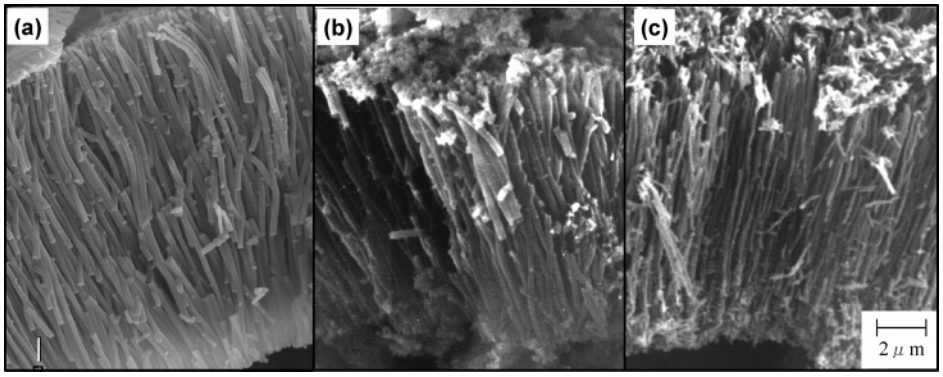

Figure 8. SEM images of V_2O_5 nanorods grown in a PC membrane with 200 nm diameter pores: (a) from $VOSO_4$ solution, (b) from $[VO_2^+]$ solution with pH change, and (c) from the sol−gel route grown on a positive electrode. (a) On a positive electrode, the reaction generates an electron: $2VO^{2+} + 3H_2O \rightarrow V_2O_5 + 6H^+ + 2e^-$. (b) On a negative electrode, the precipitate reaction proceeds according to the rising local pH; $2VO_2^+ + H_2O \rightarrow V_2O_5 + 2H^+$. (c) On the positive electrode, electrophoretic deposition occurs (zeta potential = 0 at pH = 1.825). (Reprinted with permission from ref 51. Copyright 2005 The Institute of Pure and Applied Physics.)

B), and V_2O_5 sol (route C). It is noticed that under otherwise comparable growth conditions, nanorods grown by electrochemical deposition had a negligible shrinkage, whereas those grown through the change of pH value showed a noticeable 15% lateral shrinkage; moreover, nanorods from sol electrophoretic deposition had a substantial lateral shrinkage of 50%. Such a significant difference in lateral shrinkage of three nanorods upon firing can be explained by their distinctively different growth mechanisms.

Figure 8 shows SEM images of V_2O_5 nanorod arrays grown in 200 nm PC membranes and fired at 485 °C for 1 h in air from three different solutions and sols by either electrochemical or electrophoretic deposition. The images show that these nanorods are arranged almost parallel to one another over a broad area; the distortion is ascribed to the deformation of PC membrane during pyrolysis. There is negligible shrinkage along the long axis, but the morphology and diameter of nanorods grown from different solutions or sol are different. Nanorods grown from A and B solutions have a uniform diameter throughout their entire length with a smooth surface, but in the case of C, nanorods have a narrower diameter and slightly rough surface. XRD patterns (not shown here) reveal that all nanorod arrays have the same crystal structure, vanadium pentoxide, after firing at 485 °C regardless of the growth methods and the initial solutions.

Figure 9 presents typical transmission electron microscopy (TEM) micrographs and selected-area electron diffraction patterns (SAED) of V_2O_5 nanorods grown from electrochemical deposition (route A) and sol electrophoretic deposition (route C), respectively. No appreciable difference among nanorods grown by three different methods was observed. Figure 9a,c shows TEM images of a V_2O_5 nanorod and SAED pattern, which clearly demonstrated the single-crystalline nature or, at least, well-textured nature of the grown nanorods with a [010] growth direction for nanorods grown from both routes. Figure 9b,d also shows high-resolution TEM images of a single V_2O_5 nanorod, in which lattice fringes are clearly visible. The spacing of the fringes was measured to be 0.207 nm for the nanorod grown from route A and 0.208 nm for the nanorod made from route C. These values are similar for different synthesis routes and correspond well with the spacing of the (202) planes at 0.204 nm. These fringes make an angle of 88.9° with the long axis

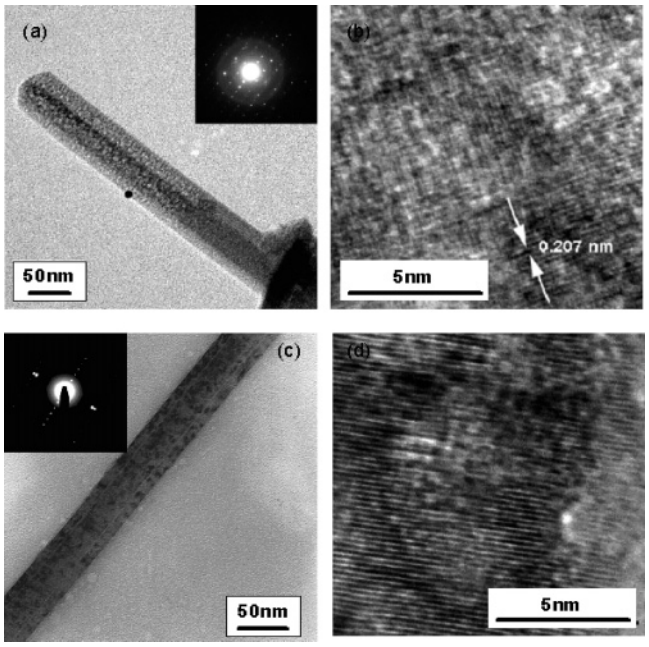

Figure 9. (a) TEM image and SAED pattern of a V_2O_5 nanorod prepared from template-based electrochemical deposition from $VOSO_4$ solution. (b) High-resolution TEM image of the V_2O_5 nanorod in part a, showing lattice fringes. The spacing of the fringes was measured to be 0.207 nm. (c) TEM image and SAED pattern of a V_2O_5 nanorod prepared from template-based electrophoretic deposition from the V_2O_5 sol. (d) High-resolution TEM image of the V_2O_5 nanorod in part c. The spacing of the fringes was measured to be 0.208 nm. The nanorods grown from both routes were demonstrated to have the single-crystalline nature or, at least, well-textured nature of the grown nanorods with a [010] growth direction. (Reprinted with permission from ref 51. Copyright 2005 The Institute of Pure and Applied Physics.)

of the nanorod, which is consistent with a growth direction of [010]. Similar measurements made on high-resolution images of other nanorods also yield results consistent with a [010] growth direction. Nanorods with the same orientation are grown from both solutions and the sol, but the formation mechanism of the single crystal is different. The formation of single-crystal nanorods from solutions, by both electrochemical deposition (route A) and pH-change-induced surface condensation (route B), is attributed to evolution selection growth as shown in Figure 10a. The initial heterogeneous nucleation or deposition on the substrate surface results in the formation of nuclei with random orientation. The subsequent growth of various facets of a

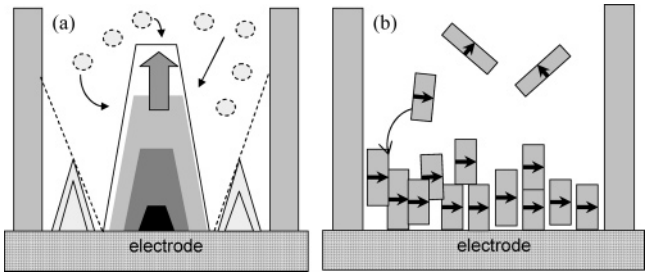

Figure 10. Schematic illustrations of growth mechanisms of single-crystalline nanorods. (a) Evolution selection growth for single-crystal V_2O_5 nanorods grown via the template-based electrodeposition; (b) homo-epitaxial aggregation for single-crystal V_2O_5 nanorods grown via the template-based electrophoretic deposition. (Reprinted with permission from ref 51. Copyright 2005 The Institute of Pure and Applied Physics.)

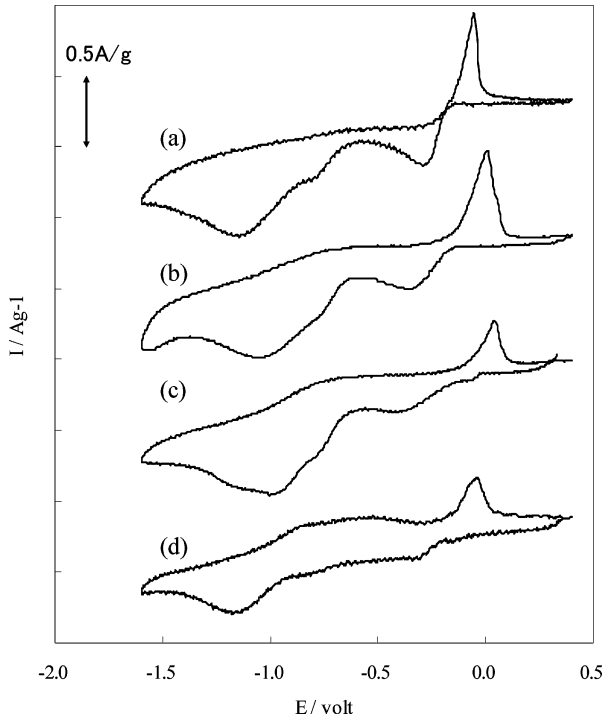

Figure 11. CVs of V_2O_5 nanorod arrays and the sol−gel film measured using a scan rate of 1 mV/s. Nanorod (a) from $VOSO_4$, (b) from pH induced, and (c) from sol−gel electrophoresis and (d) the sol−gel film. (Reprinted with permission from ref 51. Copyright 2005 The Institute of Pure and Applied Physics.)

nucleus is dependent on the surface energy and varies significantly from one facet to another.[133] In the case of nanorods made from the sol by electrophoretic deposition (route C), the formation of single-crystal nanorods is explained by so-called homoepitaxial aggregation of crystalline nanoparticles as shown in Figure 10b. Thermodynamically it is favorable for the crystalline nanoparticles to aggregate epitaxially; such a growth behavior and mechanism have been well-reported in the literature.[134,135]

Figure 11 shows typical cyclic voltammograms (CVs) of V_2O_5 nanorod arrays and a sol−gel film measured using a scan rate of 1 mV/s. The CV of nanorod arrays shows cathodic peaks at −0.3 V and −1.1 V, which correspond to Li^+ intercalation, one anodic oxidation peak at 0.0 V, and one broad anodic peak at −0.7 V, which is attributed to Li^+ extraction. Masetti et al.[136] also reported the similar CV curves which have a combination of one obvious anodic peak and two cathodic peaks. For sol−gel films, besides the anodic

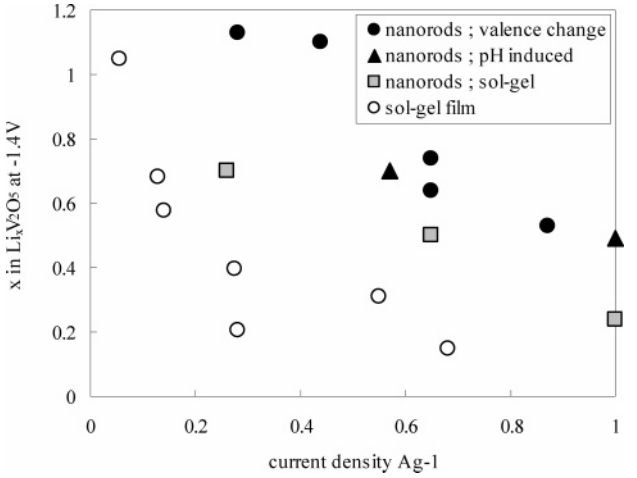

Figure 12. Plot of discharge capacity versus current density for the sol−gel derived V_2O_5 films and three types of V_2O_5 nanorod arrays grown via electrophoretic deposition from V_2O_5 sol, electrochemical deposition with valence change from VO_2^+ solution and deposition induced by local pH change from VO_2^+ solution. (Reprinted with permission from ref 51. Copyright 2005 The Institute of Pure and Applied Physics.)

peak at 0.0 V, another anodic peak at −0.7 V is apparently observed; further, the cathodic peaks at −0.3 and −1.1 V are less distinct. The integrated areas of the CV curves for the nanorod array and sol−gel film are similar, which implies that both nanorod arrays and films possess the same specific energy at this scan rate. However, extraction and intercalation kinetics are different as evidenced by the sharp peaks from the solution route as compared to far less distinctive peaks in the CV curve of the sol−gel film. The behavior of the CV curve of the nanorod array made from the sol (route C) is between that of the nanorod arrays grown from solutions (route A and B) and that of the sol−gel film, although the nanorods made from all three routes are single-crystalline.

Figure 12 shows the comparison between the current density and Li^+ intercalation capacity of nanorod arrays and sol−gel films measured by chronopotentiograms (CPs). In general, for a given Li^+ intercalation capacity, for example, $Li_{0.7}V_2O_5$, nanorod arrays from solution route possess an up to five times larger current density than that of sol−gel films, which is larger than that of the sol electrophoresis nanorod. Similarly for a given current density, such as 0.7 A/g, nanorod arrays can store up to five times more Li than in sol−gel films and more than in the sol electrophoresis nanorod. The differences in electrochemical properties observed in vanadium pentoxide nanorod arrays and films are attributed to the differences in microstructure and nanostructure. V_2O_5 nanorods grown by electrochemical deposition from solutions (route A and B) are dense single crystals, with layers parallel to the nanorod axis. Such a structure is extremely favorable to Li^+ intercalation and extraction, because the surface oxidation and reduction reactions occur along the surface of the nanorods and the solid-state diffusion distance is very small, ∼100 nm, half of the diameter of the nanorods. In addition, such structure permits the most freedom for dimensional change that accompanies intercalation and extraction reactions. Such well-aligned structure will also enhance the Li^+ diffusion through the solvent. The nanorod grown from sol electro-

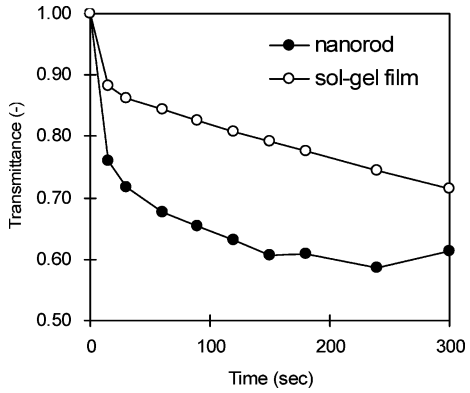

Figure 13. Change of transmittance intensity of nanorod arrays and sol−gel films versus time as a result of the lithium intercalation when submerged in Li^+ electrolyte solution under an externally applied electric field of 3 V. (Reprinted with permission from ref 52. Copyright 2005 Institute of Physics.)

phoresis (route C) is also single-crystalline and well-aligned, but it has many defects inside the crystal. That may cause the difference between these nanorod array electrodes. Sol−gel derived V_2O_5 films are polycrystalline and consist of platelet V_2O_5 grains with [001] perpendicular to the substrate surface. Therefore, the Li^+ intercalation and extraction processes will comprise of Li^+ diffusion through grain boundaries, oxidation and reduction reactions at the surface of individual crystal grains, and diffusion inside individual grains. Thus the difference in microstructure will have similar effects on the kinetics charge transport.

V_2O_5 is also an electrochromic material that exhibits a reversible optical change between the transparent state and the colored state upon extraction and intercalation of lithium ions.[137] Figure 13 shows the change of transmittance intensity at 700 nm as a function of time when an external voltage of 3.0 V is applied for the V_2O_5 nanorod array grown by electrophoretic deposition from the sol and the sol−gel derived V_2O_5 film, resepectively. A 30% reduction was achieved in ~50 s in the V_2O_5 nanorod array; however, 300 s were required in the film. The transmittance change of the nanorod array reached saturation in 3 min, while the sol−gel derived film was not yet saturated in 5 min. Extrapolation from the data in Figure 13 suggests that the sol−gel film will require at least 10 min to reach the same saturation, that is, the sol−gel film has a three times slower responding speed than the nanorod array. In conclusion, both the extent and the speed of change in the transmittance intensity of the nanorod array are significantly faster than those of the sol−gel derived film, corroborating with an enhanced electrochemical intercalation process in nanorod arrays due to a large surface area for the surface redox reaction and a short and easy diffusion path for mass and charge transport.

4.3. Nanotube and Nanocable Arrays of Vanadium Oxide. Compared to nanorods, nanotubes possess several different areas of contact, that is, the inner and outer wall surfaces as well as the open ends. In principle, nanotube arrays have an even larger surface area than nanorod arrays. In addition, the tubes can operate as electrolyte-filled channels for faster transport of the ions to the intercalation sites. The first successful approach to make a tubular vanadium oxide was with the use of carbon nanotubes as a template.[138] It was possible by exploitation of surface-tension

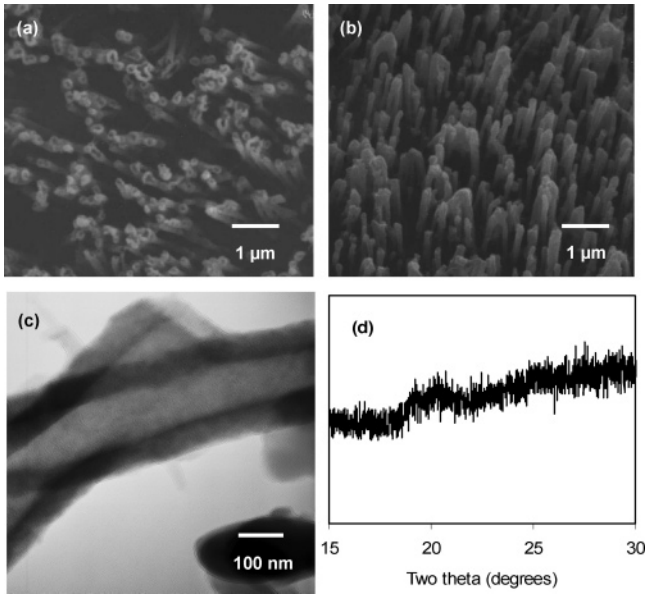

Figure 14. SEM images of (a) top view and (b) side view of V_2O_5 nanotubes electrochemically deposited within 200-nm-diameter pores of the PC membrane after the membrane dissolved away in methylene chloride. (c) TEM micrographs of isolated V_2O_5 nanotubes. (d) XRD pattern of the electrochemically prepared V_2O_5 film on the Au electrode. (Reprinted from ref 53. Copyright 2005 American Chemical Society.)

effects to coat the carbon nanotubes externally with crystalline layers of a V_2O_5-like structure. We have also prepared nanotube arrays of $V_2O_5 \cdot nH_2O$ through the template-based electrodeposition method from VO^{2+} solution by using lower voltage and shorter deposition time compared to the conditions for preparing nanorod arrays.[53] Figure 14 shows SEM images of the (a) top view and (b) side view of V_2O_5 nanotube arrays grown within the pores of the PC membrane after the membrane is dissolved away in methylene chloride. These nanotubes stand apart from each other and project straight up from the substrate surface, with a length of 10 μm (image not shown). As can be seen from the TEM images in Figure 14c, the outer diameter of the nanotube is about 200 nm and the inner diameter of the nanotube is about 100 nm. No electron diffraction pattern in TEM was observed, which suggests the amorphous nature of these nanotubes. XRD analysis of nanotube arrays shows its amorphous state as well. The possible mechanism of the nanotube growth is discussed as follows. A very thin coating of the Au−Pd alloy on the PC membrane results in a coating of metal on the edges of the pores, leading to high current density on these edges, where electrochemical reaction and deposition are initiated. On the edges of the pores, the ionic cluster, VO^{2+}, is oxidized to deposit V_2O_5 through the following reaction:

$$2VO^{2+} + 3H_2O \rightarrow V_2O_5 + 6H^+ + 2e^- \quad (2)$$

Simultaneously a reduction reaction occurs at the counter electrode:

$$2H^+ + 2e^- \rightarrow H_2(g) \quad (3)$$

Figure 15a shows the first three voltammetric cycles of the $V_2O_5 \cdot nH_2O$ nanotube arrays in the potential range between −1.6 and 0.4 V versus Ag/Ag^+ and using a scan

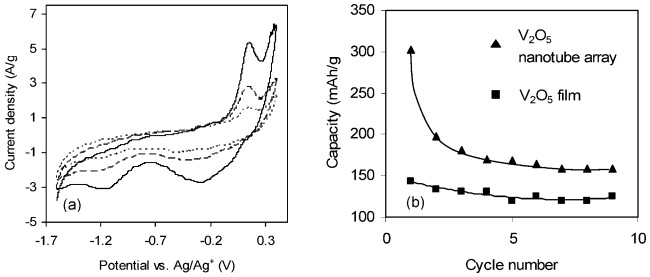

Figure 15. (a) CVs of the V_2O_5 nanotube array in a potential range of −1.6 to +0.4 V vs Ag/Ag^+ and under the scan rate of 10 mV/s. Solid line, the first cycle; dashed line, the second cycle; and dotted line, the third cycle. (b) Dependence of the discharge capacity on the cycle number obtained from chronopotentiometric measurements at a 0.4 V to −1.5 V cutoff voltage vs Ag/Ag^+. (Reprinted from ref 53. Copyright 2005 American Chemical Society.)

rate of 10 mV/s. The CV of the nanotube arrays shows cathodic peaks at −0.3 and −1.2 V, corresponding to Li^+ intercalation, and anodic oxidation peaks at 0.17 and 0.4 V, which are attributed to Li^+ extraction. It can be seen from Figure 13a that these cathodic and anodic peaks become more flattened and the area of the voltammogram shrinks under the electrochemical redox cycles, indicating the material loses some electroactivity. The degradation may be either ascribed to the electrochemically deposited $V_2O_5 \cdot nH_2O$ itself or due to the fragile structure of teh nanotubes. Consistent with CVs, CPs have shown that nanotube arrays exhibit degradation in electrochemical performance as well, and the quantitative results of the capacities calculated from chronopotentiometric measurements are discussed as follows. Figure 15b illustrates the dependence of the discharge capacity on the cycle number of both the nanotube array and the film prepared from the electrochemical deposition method. The capacity of the nanotube array is calculated on the basis of the outer diameter of 200 nm, the inner diameter of 100 nm, the length of 10 μm, and the density of 2.87 g/cm^3.[139] The $V_2O_5 \cdot nH_2O$ nanotube arrays demonstrate an initial high capacity of 300 mA·h/g, about twice the initial capacity of 140 mA·h/g from the $V_2O_5 \cdot nH_2O$ film. Such enhancement of capacity is due to the large surface area and short diffusion distances offered by the nanotube array. However, the capacity of the nanotube array decayed to 200 mA·h/g in the second cycle and 180 mA·h/g in the third one. The degradation is slower in the further cycles and finally reaches a stabilized capacity of 160 mA·h/g after the sixth cycle which is about 30% higher than the stabilized capacity of the $V_2O_5 \cdot nH_2O$ film. The initial degradation of the $V_2O_5 \cdot nH_2O$ film suggests that $V_2O_5 \cdot nH_2O$ itself prepared from electrochemical deposition has some drawback and suffers a slight loss of electroactivity during cycling. However, the nanotube array shows a more drastic decay of initial performance compared to the film during cycling, possibly due to the morphological flexibility and fragility of nanotubes, which has been speculated in the literature as well.[49]

Further, a two-step electrodeposition method has been used to prepare $Ni-V_2O_5 \cdot nH_2O$ core−shell nanocable arrays.[54] Ni nanorod arrays were first grown by template-based electrochemical deposition. In the second step, the hydrated vanadium pentoxide shell was deposited onto the surface of nickel nanorods through sol electrophoretic deposition. Figure

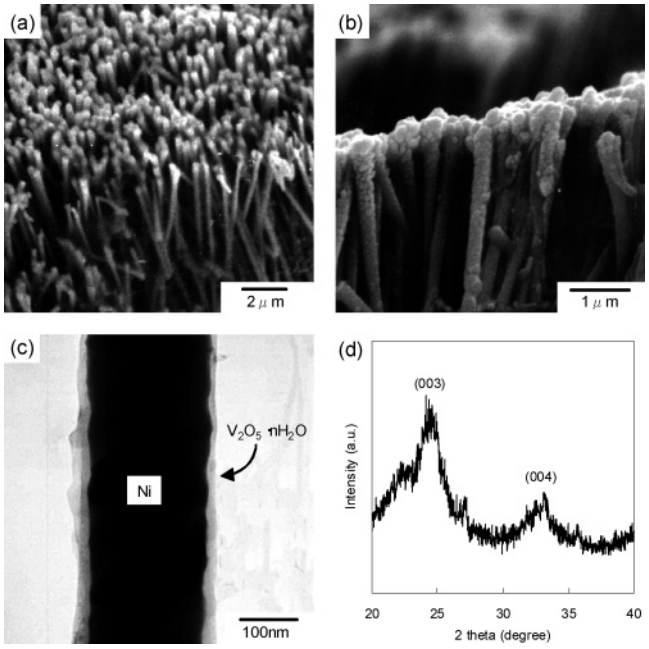

Figure 16. SEM image of (a) Ni nanorod arrays grown in 200 nm PC membranes under an applied voltage of 2.0 V and dissolving PC membrane in ethylene chloride, and (b) V_2O_5 coated Ni nanorods under an applied voltage of −0.8 V. (c) TEM micrograph of a $Ni-V_2O_5$ core−shell nanocable. (d) XRD pattern of a V_2O_5 film grown by sol electrophoretic deposition. (Reprinted from ref 54. Copyright 2005 American Chemical Society.)

16 shows typical SEM images of (a) Ni nanorod arrays grown in 200 nm PC membranes under an applied voltage of 2.0 V after the PC membrane dissolved in ethylene chloride and (b) $Ni-V_2O_5 \cdot nH_2O$ core−shell nanocable arrays with the $V_2O_5 \cdot nH_2O$ layer deposited under an applied voltage of −0.8 V. Ni nanorod arrays grown by electrochemical deposition have a diameter of ∼200 nm and stand perpendicular to the substrate. Figure 16c shows a TEM micrograph of a $Ni-V_2O_5 \cdot nH_2O$ core−shell nanocable. The image of the nanocable consists of a dark area in the center and a light area outside along the axis. This morphology clearly suggests that the nanocable has a layered structure with a different composition along the radial, and the dark area is likely to be Ni with the outer area being $V_2O_5 \cdot nH_2O$. The core material is covered completely and uniformly by a $V_2O_5 \cdot nH_2O$ shell with a thickness ranging from 30 to 50 nm based on SEM and TEM. It should be noted that the interface between Ni and $V_2O_5 \cdot nH_2O$ is not smooth microscopically, which may be attributable to the Ni nanorod nature formed by electrochemical deposition. XRD analyses of nanocable arrays revealed the presence of Ni only. The $V_2O_5 \cdot nH_2O$ coating is too thin to be detected, although energy-dispersive spectrometry analyses unambiguously revealed the presence of vanadium and oxygen. Figure 16d is the XRD pattern of the $V_2O_5 \cdot nH_2O$ film grown by electrophoretic deposition from the same sol and identical voltage, suggesting the coating layer being $V_2O_5 \cdot nH_2O$.

Figure 17a compares the CVs of the $Ni-V_2O_5 \cdot nH_2O$ nanocable arrays and the single-crystal V_2O_5 nanorod arrays, which unambiguously demonstrated better electrochemical properties of $Ni-V_2O_5 \cdot nH_2O$ nanocable arrays as compared to single-crystal V_2O_5 nanorod arrays. Figure 17b summarizes the Li^+ intercalation capacity as a function of current density

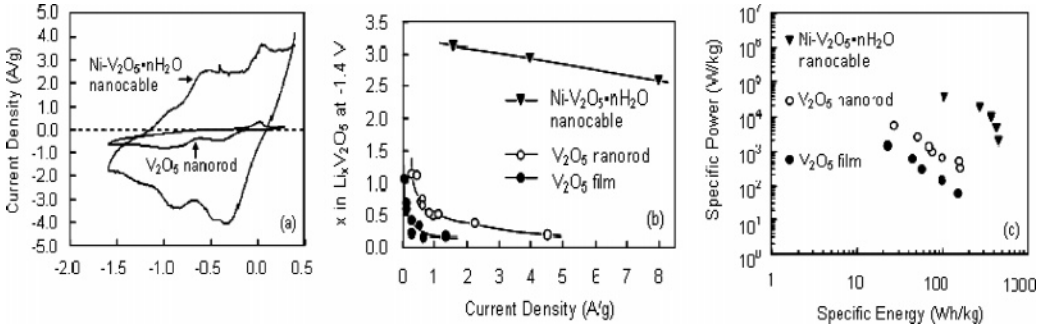

Figure 17. (a) CVs using a scan rate of 10 mV/s, (b) relationship between current density and moles of Li intercalated per mole of V_2O_5 calculated from chronopotentiometric measurements, and (c) Ragone plot, for the Ni−V_2O_5·*n*H_2O nanocable array and V_2O_5 nanorod array and film, respectively. (Reprinted from ref 54. Copyright 2005 American Chemical Society.)

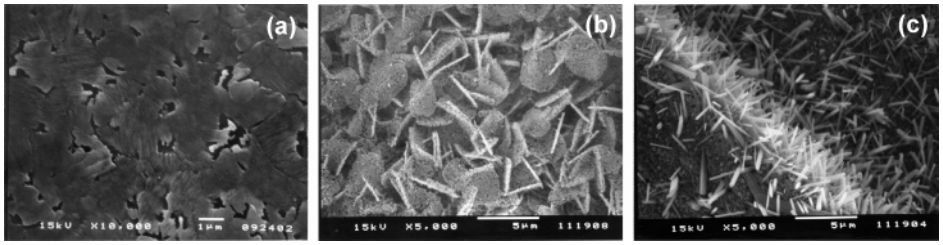

Figure 18. SEM micrographs of as-prepared V_2O_5 thin films: (a) plain structured film, (b) in situ grown platelet structured film, and (c) in situ grown fibrillar structured film. (Reprinted from ref 140. Copyright 2005 American Chemical Society.)

for Ni−V_2O_5·*n*H_2O nanocable arrays, single-crystal V_2O_5 nanorod arrays, and V_2O_5 films. The intercalation capacities of both nanorod arrays and sol−gel films decrease rapidly as the current density increases, while nanocable arrays are able to retain the high intercalation capacity at high current density (discharge rate), indicating the excellent high-rate performance of nanocable arrays. Figure 17c shows that the Ni−V_2O_5·*n*H_2O nanocable array has significantly more enhanced energy density and power density than those of the nanorod array and sol−gel film by at least 1 order of magnitude.

4.4. Nanostructured Films of Vanadium Oxide with Various Features. Platelet and fibrillar structured V_2O_5 films have been prepared by solution methods, and the discharge capacities and cyclic performance of these films were compared with those of the conventional plain structured film.[140] The platelet film consists of 20−30 nm sized V_2O_5 particles with random orientation, whereas fibrillar film is comprised of randomly oriented fibers though most of them protrude from the substrate surface. The initial discharge capacities of platelet and fibrillar structured V_2O_5 films are 1240 and 720 mA·h/g, respectively, which are far larger than the initial discharge value (260 mA·h/g) of the plain structure film. Such large discharge capacity values are ascribed to the combined effects of the reduced Li^+ diffusion distance, which prevents concentration polarization of Li^+ in the V_2O_5 electrode and poor interlayered cross-linking offering more Li^+ intercalation. However, platelet and fibrillar structured V_2O_5 films were easily degraded during electrochemical cyclic tests. Figure 18 shows the SEM observation of the surface morphology of the resulting films. The V2O5 film made from the V_2O_5 sol (see Figure 18a) shows a typical smooth surface morphology with some voids throughout the film. The film prepared by using $VOSO_4$ shows a randomly oriented platelet-like morphology with most platelets standing almost vertically and commonly having a thickness of 20−30 nm as shown in Figure 18b. Figure 18c shows the film prepared using VO^{2+} solution, and the film shows an assembly of fibrillar particles of 20−40 nm in diameter protruding from the current collector surface like the bristles of a brush.

4.5. Nanorolls and Nanobelts of Vanadium Oxide. A fundamentally new type of vanadium oxide nanorolls was prepared in a sol−gel reaction of vanadium oxide precursor conducted in the presence of an amine and followed by hydrothermal treatment.[141−145] The vanadium oxide precursor can be vanadium alkoxide or a low-cost source such as V_2O_5, $VOCl_3$,[146,147] or HVO_3.[148] The amine has long alkyl chains and functions as a molecular and structure directing template; typical templates are monoamines ($C_nH_{2n+1}NH_2$ with $4 \le n \le 22$) or diamines ($H_2N[CH_2]_nNH_2$ with $14 \le n \le 20$), or even aromatic amine such as phenylpropylamine.[149] The resultant material is black in color and easily available in high yield. There is a relatively large amount of organic template built into the oxide structure during hydrothermal synthesis, for example, $VO_{2.45}(TEMP)_{0.34}$ when the template (TEMP) is $C_{16}H_{33}NH_2$. There is a slight reduction of vanadium(V) during hydrothermal reaction, leading to a small fraction (∼5%) of vanadium(IV) in addition to vanadium(V) in the material. Therefore, the material is represented by VO_x (vanadium oxide).

As seen from the TEM image in Figure 19a, the VO_x nanorolls with the composition of $VO_{2.45}(TEMP)_{0.34}$ (TEMP = $C_{16}H_{33}NH_2$) have open ends, consisting of several concentric shells, each about 2.8−3 nm in thickness. The nanoroll is either constructed in closed concentric cylinders (nanotubes) or formed by scrolling one or more layers (nanoscrolls) as shown in Figure 19b. The outer diameters of the VO_x nanorolls range from 15 to 150 nm, and lengths are in the range of 0.5−15 μm. It is interesting to note that nanorolls obtained with monoamines tend to form thin walls that comprise rather few layers (2−10), whereas diamines

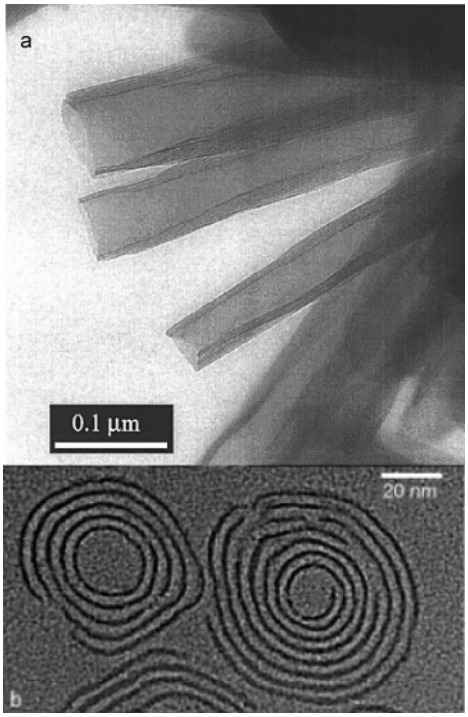

Figure 19. TEM images of (a) $C_{16}-VO_x$ nanorolls. (b) Cross-sectional structure of $C_{16}-VO_x$ nanorolls: the nanoroll on the left is nanotube composed of five concentric VO_x layers, and that on the right is the nanoscroll with gaps at several sites in the layers. (Reprinted with permission from ref 49. Copyright 1999 Electrochemical Society.)

predominantly lead to nanorolls with relatively thick walls consisting of more than 10 layers. XRD patterns of VO_x nanorolls show the highly intense and sharp *00l* reflections at low scattering angles that are characteristic of a well-ordered layered structure. The interlayer distances of these reflections range from 1.7 to 3.8 nm and increase linearly with the size of the amine molecules. This indicates that protonated template molecules are embedded between the VO_x layers, and interlayer distances between approximately 1.7 and 3.8 nm can be achieved in a controllable way. Less intense and broad *hk*0 reflection peaks appear at higher scattering angles in the XRD patterns of VO_x nanorolls, indicating a two-dimensional square lattice with a length of about 0.62 nm. The positions of the *hk*0 peaks are not influenced by the template size, indicating that different templates have no influence on the wall structure. All experimental evidence and structural simulation show that the VO_x layers have the composition V_7O_{16}. The layers are composed of two sheets of VO_5 square pyramids connected by VO_4 tetrahedra and pointing in the opposite direction.[150,151]

Pillai et al. have prepared a new type of vanadium oxide nanoroll (nanotube) by applying ammonia during the hydrolysis step of the synthesis.[152] The resultant nanotubes have alternating interlayer distances, and such a unique structure is first observed in a tubular phase. Figure 20a shows the cross-sectional TEM image of the nanotube. The diameter of the tube is around 200 nm and is much larger than that conventional nanotubes. The tube wall is relatively thin and consists of two different, alternating, interlayer distances as shown in Figure 20b. It is assumed that amine molecules are located in the wide layers, and the comparatively smaller NH_4^+ ions are embedded in the narrow separation. The

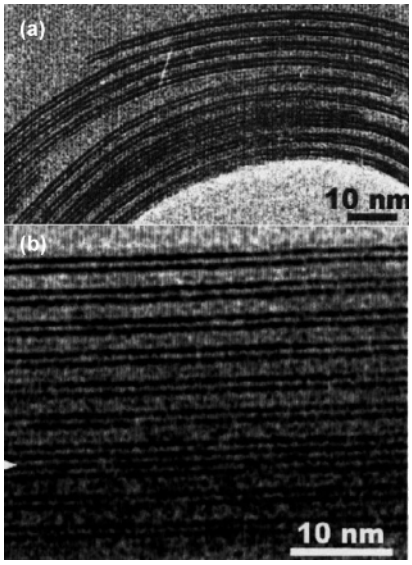

Figure 20. TEM images of VO_x nanorolls with two different interlayer spacings (~0.9 nm and ~2.0 nm; template, dodecylamine): (a) cross-sectional structure of the tube showing the bending and (b) a closer look at the tube wall. (Reprinted with permission from ref 152. Copyright 2001 Elsevier.)

narrower interlayer distance makes the tube structure stiffer than that with only amine molecules. This stiffer structure makes rolling and bending difficult and thus results in the larger diameter of these tubes compared to the VO_x nanorolls with evenly separated interlayers.

In comparison with other tubular systems, the VO_x nanorolls are especially interesting because they possess four different contact regions, that is, tube opening, outer surface, inner surface, and interstitial region. Therefore, the VO_x nanorolls are very promising for the realization of highly functional and effective nanodevices such as sensors, single-electron transistors, and energy storage/release systems. VO_x nanorolls can intercalate a variety of molecules and ions reversibly without change in the crystalline structure. Various metal ions, for example, Na^+, K^+, Ca^{2+}, Sr^{2+}, Fe^{2+}, or Co^{2+}, can be intercalated into VO_x nanorolls to substitute the monoamine molecules embedded in the interlayer structure.[153] Even diamines can be intercalated into the interlayer structure to replace the monoamines simply by mixing with a suspension of the VO_x nanorolls.[154] Intercalated monoamines can be substituted by diamines simply.[154] More specifically, intercalation of lithium ions into VO_x nanorolls have been studied intensely recently[49,155,156] and opens up some new perspectives for battery applications. The discharge capacities have been found up to 200 mA·h/g; however, there is structural breakdown during redox cycles and degradation in cycling performance due to the morphological flexibility.

In most cases, VO_x nanorolls show defects such as gaps in the VO_x layers inside the walls.[157] Sun et al. have recently investigated the relationship between the synthesis chemistry, the nanoscale structure, and the electrochemical performance of vanadium oxide nanorolls.[158] The VO_x nanorolls exhibit different morphologies and properties depending upon the synthetic conditions. Higher reducing conditions yield nearly perfect nanorolls showing no oxide cracks in the walls, whereas less reducing conditions produce defect-rich nanorolls with many cracks in the walls. Both types of nanorolls

then undergo ion-exchange reactions to replace the templating ammonium ions with Na^+, followed by electrochemical characterizations to examine the Li^+-intercalation performance. The cyclic voltammetry measurements show that the well-ordered nanorolls behave closely to classic crystalline vanadium pentoxide, while the defect-rich nanorolls have electrochemical behavior similar to that of sol−gel-prepared hydrated vanadium pentoxide materials whose crystalline order is restricted to nanoscale. The specific capacity of defect-rich nanorolls (340 mA·h/g) is higher than that of the well-ordered nanorolls (240 mA·h/g) under comparable conditions. Furthermore, the defect-rich nanorolls demonstrate better cycling performance. The enhanced capacity in defect-rich nanorolls is ascribed to the additional redox sites resulted from the nanoscale disorder. The cracks and shedding in the defect-rich nanorolls also lead to increased accessibility of lithium ions to the interlayer regions and thus result in the improved cycling performance. In conclusion, VO_x nanorolls may find a bright future as high-performance cathode materials by modifying the morphology and structure.

Owing to the layered structure, vanadium pentoxide and especially hydrated vanadium pentoxide that has larger interlayer spacing allow gas molecules to enter and approach the active position easily, thus finding applications as sensor materials. For example, alcohol gases containing hydroxyl groups can be adsorbed on V−O layers by hydrogen bonds and then react with the negative oxygen to change the conductivity of the sensors. Biomedical, chemical, and food industries have a strong demand on alcohol sensors with high selectivity and stability for breath analysis or wine-quality monitoring. Conventional ethanol sensors are mostly based on SnO_2, ZnO, TiO_2, and Fe_2O_3 and usually suffer from cross-sensitivity to other gases, low long-term stability, a need for high working temperature, or a lack of high sensitivity to lower-level ethanol vapor.[159] Therefore, some new types of ethanol-sensing materials are still being studied and developed. One-dimensional nanostructures of various metal oxides have been synthesized and investigated for gas sensors.[160−163] Specifically, nanobelts of oxides are very promising for sensors due to the high surface-to-volume ratio and single-crystalline nature.[164,165]

Pan et al. used a hydrothermal method to synthesize long beltlike nanowires, which are several tens of micrometers long and a few tens of nanometers wide, and are crystallized well growing along the [010] direction.[166] A hydrothermal method was later used by Schlecht et al. to synthesize new types of vanadium oxide belts exhibiting a boomerang shape.[167] A layered structure was revealed closely corresponding to that in known vanadium pentoxide nanofibers. The structure of nanobelts is unique in that it originates from twinning along the [130] direction, which is the first observation of twins within individual nanosized crystals. However, the intercalation properties of these beltlike nanowires or boomerang-shaped nanobelts of vanadium oxides are not further investigated. Liu et al. have recently synthesized vanadium pentoxide nanobelts for highly selective and stable ethanol sensor materials.[21] The nanobelts were prepared by acidifying ammonium metavanadate followed by hydrothermal treatment. The XRD pattern for the vanadium pentoxide nanobelts displays a set of peaks characteristic of 00*l* reflections, indicating the hydrated phase $V_2O_5{\cdot}nH_2O$ with water embedded between the layers. The layer spacing is calculated to be 10.92 Å from the 001 reflection peak. Figure 21a presents the SEM image of $V_2O_5{\cdot}nH_2O$ nanobelts, showing that the belts are tens of micrometers long and 60−100 nm wide. Figure 21b shows the TEM image of a few nanobelts, clearly revealing the short side of the rectangular cross section near the twist of one nanobelt and the thickness of the nanobelt being around 10−20 nm. As seen from Figure 21c, both the high-resolution TEM image and the corresponding SAED pattern unambiguously show that the nanobelts are single-crystalline, growing along the [010] direction. The belts are somewhat rigid and thus cannot be rolled up but only bent, as indicated in Figure 21a.

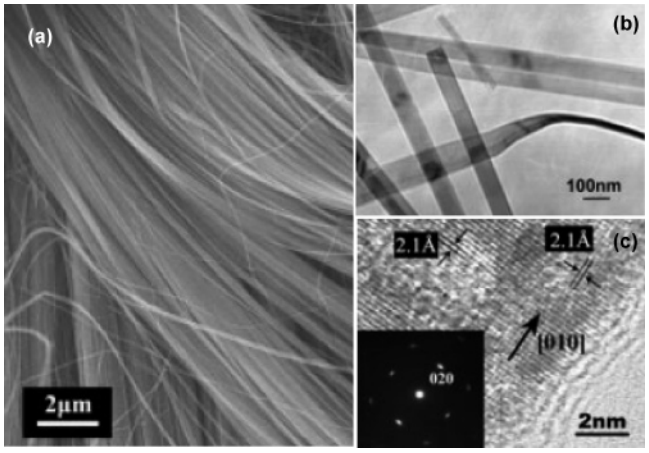

Figure 21. (a) SEM image of $V_2O_5{\cdot}nH_2O$ nanobelts, (b) TEM image of $V_2O_5{\cdot}nH_2O$ nanobelts, and (c) high-resolution TEM image of a single $V_2O_5{\cdot}nH_2O$ nanobelt with the electron diffraction pattern shown in the inset. (Reprinted with permission from ref 21. Copyright 2005 Wiley-VCH.)

A common surfactant, CTAB (cetyltrimethylammonium bromide), was added to the initial reaction solution to improve the flexibility of the belts. The layer spacing of the CTAB-intercalated−$V_2O_5{\cdot}nH_2O$ nanobelts is enlarged to 34.78 Å. The nanobelts are slightly wider than the CTAB-free product but can roll up randomly with a ring-like morphology as a result of their improved flexibility. Such nanobelts are assumed to have more active positions exposed and are expected to have better properties. The third type of "nanobelts" is prepared by annealing $V_2O_5{\cdot}nH_2O$ nanobelts at 400 °C in air, leading to an orthorhombic phase. The resultant product loses the belt shape by forming rodlike structure and is thus stiffer. There are also cracks formed because of loss of coordinated water.

In the gas-sensing measurements, all the three types of gas sensors based on vanadium pentoxide, that is, $V_2O_5{\cdot}nH_2O$ nanobelts, $V_2O_5{\cdot}nH_2O$−CTAB nanobelts, and V_2O_5 nanorods, have an optimal sensitivity to ethanol in the working temperature range 150−400 °C. Isothermal response curves at 200 °C show that all three sensor materials provide a better response and quicker response/recovery time than those reported in the literature.[168] Specifically, $V_2O_5{\cdot}nH_2O$ sensors exhibit higher sensitivity to low ethanol concentrations (<10 ppm), whereas the $V_2O_5{\cdot}nH_2O$−CTAB and V_2O_5 are more sensitive to high concentrations. Moreover,

the selectivity of the vanadium pentoxide is also tested for practical purposes. It is found that the sensors are insensitive to CO and H_2 and the responses to H_2S, NH_3, H_2, C_3H_8, CO, and NO_x are lower than the response to ethanol. It is expected that metal ion doping or organic template modification can further enhance the sensitivity of nanobelts of vanadium pentoxide as sensor materials.

4.6. Self-Assembly of Vanadium Oxide Nanowires. In addition to template synthesis and the hydrothermal route, one-dimensional nanostructures of vanadium pentoxide can grow spontaneously in the sol. The drawback of this method is that it takes a longer time; however, the V_2O_5 nanowires in the sol are negatively charged, and this property leads to novel processes of self-assembly and patterning for applications in nanodevices.

It has been known for a long time that colloids of vanadium pentoxide have the fibrous structure.[169,170] Under an electric field or a shear stress, the V_2O_5 colloidal sols become anisotropic. V_2O_5 sols show amazing properties such as thixotropy and rheopexy[171,172] and are often used as models to investigate the optical birefringence[173] or the hydrodynamic behavior.[174] In the sol made from vanadic acid aqueous solution, tiny threads of vanadium pentoxide about 2 nm wide and 100 nm long are formed first.[175] These threads grow lengthwise, and the subsequent self-assembly edge-to-edge results in ribbonlike wires. Such growth can be explained by a condensation mechanism.[176] Typically, gels of vanadium pentoxide are composed of ribbonlike nanowires about 10 nm wide and over 1 μm long.[177]

Chang et al. recently reported growth conditions of V_2O_5 nanowires and demonstrated a simple but noble percolation system composed of the conducting nanowires and insulating matrix.[48] V_2O_5 nanowires were prepared from ammonium (meta)vanadate with acidic ion-exchange resin. The length of V_2O_5 nanowires can be increased by polycondensation of vanadic acid in deionized water. As the reaction proceeded at room temperature, the lengths of the V_2O_5 nanowires increased at a speed of 0.13 μm/day at an early stage of the growth and 0.03 μm/day on the average up to 3 months. The percolation network was made by abruptly freezing the homogeneously dispersed aqueous solutions of V_2O_5 nanowires in liquid nitrogen. After 7 h of aging time, an abrupt increase of the conductance was observed, revealing the satisfaction of the percolation threshold ($P_c \sim 0.17$) at the average wire length of 40 nm.

The idea of using V_2O_5 for converting electrical energy to mechanical energy has been considered for more than 10 years.[178] This idea was first realized by Gu et al. who successfully prepared electrochemical actuators (artificial muscles) based on V_2O_5 nanowires.[45] V_2O_5 nanowires were obtained from the sol synthesized by mixing ammonium *meta*-vanadate and acidic ion-exchange resin in water. The SiO_2/Si substrate was pretreated with (3-aminopropyl)-triethoxysilane (APTES) to generate positively charged ammonium groups on the surface to adsorb negatively charged V_2O_5 nanowires through ionic interaction. The resultant sample is an entangled network of V_2O_5 nanowires. Furthermore, free-standing sheets of V_2O_5 nanowires were prepared by filtering the sol of nanowires through a cellulose nitrate filter using a water aspirator. This procedure produced a brown sheet which was rinsed with water and then peeled off the filtrer paper, resulting in a free-standing sheet composed of entangled V_2O_5 nanowires. The nanowire sheet was heated at 80 °C to increase the flexibility and cause dehydration. The morphology of the resultant sheet looks similar to that of the sheet of single-walled carbon nanotubes used in the actuator.[179] Electromechanical actuation was demonstrated for a V_2O_5 nanowire sheet immersed in an aqueous electrolyte. It was found that the V_2O_5 nanowire sheets provide a high Young's modulus, high actuator-generated stress, and high actuator stroke at low applied voltage. Electrochemical charge injection and intercalation that causes the electromechanical actuation are made faster due to the high surface area of these V_2O_5 nanowire sheets. The actuation strain was observed to be 0.21%, and the force-generation capability was 5.9 MPa; additionally, the V_2O_5 nanowire sheets require much lower applied voltages than commercial ferroelectric and electrostrictive materials. Thus, the V_2O_5 nanowire sheets open up a new perspective for redox-dependent application of V_2O_5 nanostructures as actuators.

Usually nanowires are synthesized in a solution or powder form. To build functional devices, individual nanowires have to be picked up and assembled onto the substrate, which cannot be achieved by conventional microfabrication strategies. However, the spontaneous growth of negatively charged V_2O_5 nanowires in the sol has stimulated some researchers to develop a simple and elegant method, the so-called "surface-programmed assembly" for high-precision assembly and alignment of pristine V_2O_5 nanowires on solid substrates.[46] In this method, positively charged surface molecular patterns are used to assemble and align a large number of V_2O_5 nanowires over a large surface area, while neutral surface molecular patterns are used to prevent adsorption of nanowires. For example, self-assembled monolayer patterns of 1-octadecyltrichlorosilane (OTS) can be created on the surface of SiO_2 substrates with photolithography first to generate the neutral regions, and the remaining area is backfilled with APTES molecules to create positively charged areas. Negatively charged nanowires of V_2O_5 are attracted onto the positively charged APTES areas, and there is no nanowire on the OTS regions, as shown in Figure 22a. Furthermore, individual nanowires can be assembled using the same process. The length of V_2O_5 can be controlled by keeping the mixture of ammonium *meta*-vanadate and acidic ion-exchange resin for a certain time period. Longer aging time leads to longer V_2O_5 nanowires in the sol, for example, nanowires a few micrometers long are obtained by keeping the mixture for 20 days. Therefore, assembly and alignment of individual nanowires on the substrates can be achieved by placing the molecular patterns in the sol, as shown in Figure 22b.

The researchers further made a transistor device based on an array of nanowires by using the conventional lift-off method to fabricate Au electrodes on the nanowire array as shown in Figure 23. The observed gating effect is in good agreement with that reported in the literature,[19] indicating

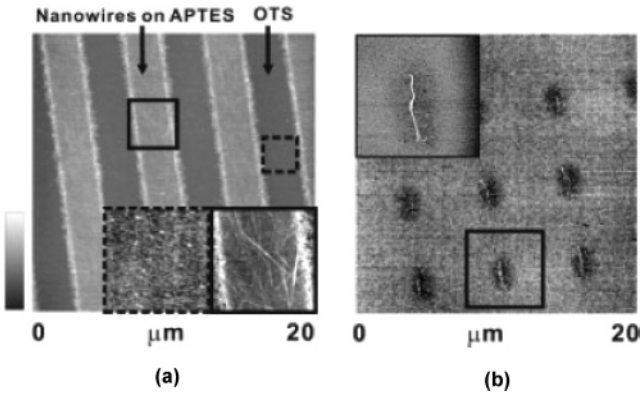

Figure 22. (a) Atomic force microscopy topography image of V_2O_5 naowires assembled on APTES patterns on SiO_2. OTS has been used for passivation. Insets show high-resolution atomic force microscopy images of the OTS (left) and APTES regions (right). (b) Atomic force microscopy topography image of individual V_2O_5 nanowires (white lines) assembled on cysteamine patterns (dark areas) on Au. ODT (1-octadecanethiol; bright areas) is used for passivation. (Reprinted with permission from ref 46. Copyright 2005 Wiley-VCH.)

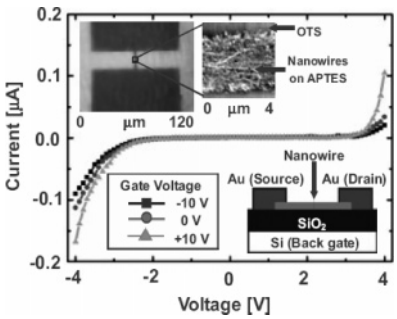

Figure 23. Gating effect of V_2O_5 nanowire transistors. The n-type Si substrate is used as a back gate. The insets show optical micrograph images of Au electrodes and an atomic force microscopy topography image of nanowire patterns connecting those electrodes. (Reprinted with permission from ref 46. Copyright 2005 Wiley-VCH.)

that the device based on the V_2O_5 nanowire pattern functions properly.

This important "surface-programmed assembly" method offers the capacity to be entirely compatible with conventional microfabrication processes and does not rely on any external force for nanowire assembly or alignment. Furthermore, purity of V_2O_5 nanowires is ensured because it is not needed to chemically functionalize the nanowires. High-precision assembly and alignment of V_2O_5 nanowire arrays can be achieved over a large area of $\sim$1 cm $\times$ 1 cm. Combination of the simplicity of this method and the versatile properties of V_2O_5 will lead to significant breakthrough toward sophisticated or multifunctional nanodevices.

5. Concluding remarks

Despite focusing on vanadium pentoxide, this review clearly reveals how moving from bulk materials to the nanoscale can significantly change their performance in devices for energy storage and conversion and for sensing and actuation. The development of nanodevices can benefit from the distinct morphology and high aspect ratio of one-dimensional anisotropic nanostructures as these can be functionalized in unique ways. Among a wide range of different synthetic methods to prepare nanomaterials, soft chemistry routes that involve sol−gel reactions and that frequently use organic molecules as structure-directing templates are simple and elegant. First, the tempalate-based method has been utilized to prepare various ordered arrays of nanostructures, including polycrystalline V_2O_5 nanorod arrays, single-crystalline V_2O_5 nanrod arrays, $V_2O_5 \cdot nH_2O$ nanotube arrays, and $Ni-V_2O_5 \cdot nH_2O$ core−shell nanocable arrays. Morphology, structure, and growth mechanisms of these nanostructures have been discussed. The Li^+-intercalation properties of the nanostructured electrodes have been compared to the film electrode of vanadium pentoxide. All nanostructured electrodes exhibit storage capacity and rate performance significantly improved over those of V_2O_5 films, as a result of the larger surface area and the shorter diffusion path. Moreover, the relationship between low-temperature performance of polycrystalline V_2O_5 nanorod arrays and the nanostructures is discussed, and the volumetric energy density of the V_2O_5 nanorod arrays can be improved by chemically etching the PC membranes prior to template synethsis. The hydrothermal route is another powerful tool for generalizing and systematizing controlled syntheses of nano-morphologies, such as VO_x nanorolls for cathode materals in lithium ion batteries and V_2O_5 nanobelts for ethanol sensor materials. Negatively charged V_2O_5 nanowires can also grow spontaneously in a sol. This simple and controlled synthesis leads to easy fabrication of robust free-standing V_2O_5 nanowire sheets for actuation function, in addition to precise assembly and patterning of V_2O_5 nanowires for nanotransistor applications. Considering that vanadium oxides possess versatile redox-dependent properties, one can foresee the possibility of fabricating multifunctional and/or hybrid nanodevices based on it. Processing methods in this review are generally applicable to fabricating nanostructures of other oxides, for example, metal oxide core−shell nanocable arrays. Discussion on the underlying principle that affects the properties of V_2O_5 in the present work can be helpful for further understanding of vanadium oxide and other transition metal oxides.

Acknowledgment. This work has been supported in part by the National Science Foundation (DMI-0455994). This work has also been supported by the Center for Nanotechnology at UW, Pacific Northwest National Laboratories (PNNL), Joint Institute of Nanoscience and Nanotechnology (JIN, UW, and PNNL), Washington Technology Center (WTC), and JFE Steel Corporation, Japan. Y.W. would like to acknowledge the Ford, Nanotechnology, and JIN graduate fellowships. A portion of the research (TEM study) described in this paper was performed in the Environmental Molecular Sciences Laboratory, a national scientific user facility sponsored by the Department of Energy's Office of Biological and Environmental Research located at PNNL.

References

(1) Cao, G. Z. *Nanostructures and Nanomaterials, Synthesis, Properties and Applications*; Imperial College Press: London, 2004.
(2) Bachtold, A.; Hadley, P.; Nakanishi, T.; Dekker, C. *Science* **2001**, *294*, 1317.
(3) Martel, R.; Schmidt, T.; Shea, H. R.; Hertel, T.; Avouris, P. *Appl. Phys. Lett*. **1998**, *73*, 2447.
(4) Zheng, G.; Lu, W.; Jin, S.; Lieber, C. M. *Adv. Mater*. **2004**, *16*, 1890.
(5) Heo, Y. W.; Tien, L. C.; Kwon, Y.; Norton, D. P.; Pearton, S. J.; Kang, B. S.; Ren, F. *Appl. Phys. Lett*. **2004**, *85*, 2274.
(6) Cui, Y.; Wei, Q.; Park, H.; Lieber, C. M. *Science* **2001**, *293*, 1289.

(7) Star, A.; Han, T.; Joshi, V.; Gabriel, J. P.; Grüner, G. *Adv. Mater*. **2004**, *16*, 2049.
(8) Comini, E.; Faglia, G.; Sberveglieri, G.; Pan, Z. W.; Wang, Z. L. *Appl. Phys. Lett*. **2002**, *81*, 1869.
(9) Snow, E. S.; Perkins, F. K.; Houser, E. J.; Badescu, S. C.; Reinecke, T. L. *Science* **2005**, *307*, 1942.
(10) Dai, H. J.; Hafner, J. H.; Rinzler, A. G.; Golbert, D. T.; Smalley, R. E. *Nature* **1996**, *384*, 147.
(11) Zhang, Y.; Suenaga, K.; Colliex, C.; Iijima, S. *Science* **1998**, *281*, 973.
(12) Karunakaran, C.; Senthilvelan, S. *J. Colloid Interface Sci.* **2005**, *289*, 466.
(13) Raju, A. R.; Rao, C. N. R. *J. Chem. Soc., Chem. Commun.* **1991**, *18*, 1260.
(14) Imawan, C.; Steffes, H.; Solzbacher, F.; Obermeier, F. *Sens. Actuators, B* **2001**, *77*, 346.
(15) Sanchez, C.; Morineau, R.; Livage, J. *Phys. Status Solidi A* **1983**, *76*, 661.
(16) Shoji, E.; Buttry, D. A. *Electrochim. Acta* **2000**, *45*, 3757.
(17) Goward, G. G.; Leroux, F.; Nazar, L. F. *Electrochim. Acta* **1998**, *43*, 1307.
(18) Lira-Cantu, M.; Gomez-Romero, P. *J. Electrochem. Soc.* **1999**, *146*, 4139.
(19) Muster, J.; Kim, G. T.; Krstic, V.; Park, J. G.; Park, Y. W.; Roth, S.; Burghard, M. *Adv. Mater*. **2000**, *12*, 420.
(20) Livage, J. *Chem. Mater*. **1991**, *3*, 578.
(21) Liu, J.; Wang, X.; Peng, Q.; Li, Y. *Adv. Mater*. **2005**, *17*, 764.
(22) Krusin-Elbaum, L.; Newns, D. M.; Zeng, H.; Derycke, V.; Sun, J. Z. Sandstrom, R. *Nature* **2004**, *431*, 672.
(23) Ŝordan, R.; Burghard, M.; Kern, K. *Appl. Phys. Lett.* **2001**, *79*, 2073.
(24) Ancona, M. G.; Kooi, S. E.; Kruppa, W.; Snow, A. W.; Foos, E. E.; Whitman, L. J.; Park, D.; Shirey, L. *Nano Lett*. **2003**, *3*, 135.
(25) O'Hare, D. In *Inorganic Materials*; Bruce, D. W., O'Hare, D., Eds.; John Wiley & Sons: New York, 1991; p 165.
(26) Schöllhorn, R. *Angew Chem., Int. Ed. Engl*. **1980**, *19*, 983.
(27) Schöllhorn, R. In *Chemical Physics of Intercalation*; Legrand A. P., Flandrois, S., Eds.; NATO Series B; Plenum: New York, 1987; Vol. 172, p 149.
(28) Murphy, D. W.; Sunshine, S. A.; Zahurak, S. M. In *Chemical Physics of Intercalation*; Legrand, A. P., Flandrois, S., Eds.; NATO Series B; Plenum: New York, 1987; Vol. 172, p 173.
(29) Murphy, D. W.; Christian, P. A.; Disalvo, F. J.; Waszczak, J. V. *Inorg. Chem*. **1985**, *24*, 1782.
(30) Clement, R. *J. Am. Chem. Soc.* **1981**, *103*, 6998.
(31) Nazar, L. F.; Jacobson, A. J. *J. Chem. Soc., Chem. Commun*. **1986**, 570.
(32) Schöllhorn, R. *Physics of Intercalation Compounds*; Springer-Verlag: Berlin, 1981.
(33) Whittingham, M. S. *Chem. Rev*. **2004**, *104*, 4271.
(34) Whittingham, M. S.; Song, Y. Lutta, S.; Zavalij, P. Y.; Chernova, N. A. *J. Mater. Chem*. **2005**, *15*, 3362.
(35) Sakurai, Y.; Okada, S.; Yamaki, J.; Okada, T. *J. Power Sources* **1987**, *20*, 173.
(36) West, K.; Zachau-Christiansen, B.; Ostergard, M. J. L.; Jacobsen, T. *J. Power Sources* **1987**, *20*, 165.
(37) West, K.; Zachau-Christiansen, B.; Jacobsen, T.; Skaarup, S. *Electrochim. Acta* **1993**, *38*, 1215.
(38) Salloux, K.; Chaput, F.; Wong, H. P.; Dunn, B.; Breiter, M. W. *J. Electrochem. Soc*. **1995**, *142*, L191.
(39) Petkov, V.; Trikalitis, P. N.; Bozin, E. S.; Billinge, S. J. L.; Vogt, T.; Kanatzidis, M. G. *J. Am. Chem. Soc.* **2002**, *124*, 10157.
(40) Coustier, F.; Hill, J.; Owens, B. B.; Passerini, S.; Smyrl, W. H. *J. Electrochem. Soc.* **1999**, *146*, 1355.
(41) Portiron, E.; Salle, A. L.; Varbaere, A.; Piffard, Y.; Guyomard, D. *Electrochim. Acta* **1999**, *45*, 197.
(42) Lantelme, F.; Mantoux, A.; Groult, H.; Lincot, D. *J. Electrochem. Soc.* **2003**, *150*, A1202.
(43) Hibino, M.; Ugaji, M.; Kishimoto, A.; Kudo, T. *Solid State Ionics* **1995**, *79*, 239.
(44) Wang, Y.; Lee, K.; Shang, H.; Wiley, B.; Xia, Y.; Cao, G. Z. *Phys. Status Solidi* **2005**, *202*, R79.
(45) Gu, G.; Schmid, M.; Chiu, P.; Minett, A.; Fraysse, J.; Kim, G.; Roth, S.; Kozlov, M.; Muñoz, E.; Baughman, R. H. *Nat. Mater*. **2003**, *2*, 316.
(46) Myung, S.; Lee, M.; Kim, G. T.; Ha, J. S.; Hong, S. *Adv. Mater*. **2005**, *17*, 2361.
(47) Kim, G. T.; Muster, J.; Krstic, V.; Park, J. G.; Park, Y. W.; Roth, S.; Burghard, M. *Appl. Phys. Lett.* **2000**, *76*, 1875.
(48) Chang, Y. J.; Kang, B. H.; Kim, G. T. *Appl. Phys. Lett.* **2004**, *84*, 5392.
(49) Spahr, M. E.; Stoschitzki-Bitterli, P.; Nesper, R.; Haas, O.; Novák, P. *J. Electrochem. Soc*. **1999**, *146*, 2780.
(50) Takahashi, K.; Limmer, S. J.; Wang, Y.; Cao, G. Z. *J. Phys. Chem. B* **2004**, *108*, 9795.
(51) Takahashi, K.; Limmer, S. J.; Wang, Y.; Cao, G. Z. *Jpn. J. Appl. Phys*. **2005**, *44*, 662.
(52) Takahashi, K.; Wang, Y.; Cao, G. Z. *Appl. Phys. Lett.* **2005**, *86*, 053102.
(53) Wang, Y.; Takahashi, K.; Shang, H.; Cao, G. Z. *J. Phys. Chem. B* **2005**, *109*, 3085.
(54) Takahashi, K.; Wang, Y.; Cao, G. Z. *J. Phys. Chem. B* **2005**, *109*, 48.
(55) Pinna, N.; Wild, U.; Urban, J.; Schlögl, R. *Adv. Mater*. **2003**, *15*, 329.
(56) Lutta, S. T.; Dong, H.; Zavalij, P. Y.; Whittingham, M. S. *Mater. Res. Bull*. **2005**, *40*, 383.
(57) Burdese, A. *Ann. Chim. (Rome)* **1957**, *47*, 795.
(58) Nihuoul, G.; Leroux, Ch.; Madigou, V.; Durak, J. *Solid State Ionics* **1999**, *117*, 105.
(59) Anderson, J. S.; Kahn, A. S. *J. Less-Common Met*. **1970**, *22*, 209.
(60) Oka, Y.; Ohtani, T.; Yamamoto, N.; Takada, T. *Nippon Seramikkusu Kyokai Gakujutsu Ronbunshi* **1989**, *97*, 1134.
(61) Hagrman, D.; Zubieta, J.; Warren, C. J.; Meyer, L. M.; Treacy, M. M. J.; Haushalter, R. C. *J. Solid State Chem*. **1998**, *138*, 178.
(62) Enjalbert, R.; Galy, J. *Acta Crystallogr., Sect. C* **1986**, *42*, 1467.
(63) Zavalij, P. Y.; Whittingham, M. S. *Acta Crystallogr., Sect. B* **1999**, *55*, 627.
(64) Murphy, D. W.; Christian, P. A.; DiSalvo, F. J.; Waszczak, J. V. *Inorg. Chem*. **1979**, *18*, 2800.
(65) Abello, L.; Husson, E.; Repelin, Y. R.; Lucazeau, G. *Spectrochim. Acta* **1983**, *39A*, 641.
(66) Winter, M.; Jürgen, O. B.; Spahr, M. E.; Novák, P. *Adv. Mater*. **1998**, *10*, 725.
(67) Murphy, D. W. In *Intercalation Chemistry*; Whittingham, M. S., Jacobsen A. J., Eds.; Academic: New York, 1982; p 563.
(68) Hyde, B. G.; Anderson, S. *Inorganic Crystal Structures*; Wiley: New York, 1989; p 16.
(69) Petkov, V.; Trikalitis, P. N.; Bozin, E. S.; Billinge, S. J. L.; Vogt, T.; Kanatzidis, M. G. *J. Am. Chem. Soc*. **2002**, *124*, 10157.
(70) Ostermann, W. *Wiss. Ind. Hamburg* **1922**, *1*, 17.
(71) Wang, Y.; Shang, H.; Chou, T.; Cao, G. Z. *J. Phys. Chem. B* **2005**, *109*, 11361.
(72) Birks, L. S.; Friedman, H. *J. Appl. Phys.* **1946**, *17*, 687.
(73) Hagrman, P. J.; Finn, R. C.; Zubieta, J. *Solid State Sci.* **2001**, *3*, 745.
(74) Owens, B. B.; Passerini, S.; Smyrl, W. H. *Electrochim. Acta* **1999**, *45*, 215.
(75) Crespi, A.; Schmidt, C.; Norton, J.; Chen, K.; Skarstad, P. *J. Electrochem. Soc*. **2001**, A30.
(76) Morcrette, M.; Rozier, P.; Dupont, L.; Mugnier, E.; Sannier, L.; Galy, J.; Tarascon, J. M. *Nat. Mater*. **2003**, *2*, 755.
(77) Morcrette, M.; Martin, P.; Rozier, P.; Vezin, H.; Chevallier, F.; Laffont, L.; Poizot P.; Tarascon, J. M. *Chem. Mater*. **2005**, *17*, 418.
(78) Whittingham, M. S. *J. Electrochem. Soc*. **1975**, *123*, 315.
(79) Cocciantelli, J. M.; Doumerc, J. P.; Pouchard, M.; Broussely, M.; Labat, J. *J. Power Sources* **1991**, *34*, 103.
(80) Galy, J. *J. Solid State Chem*. **1992**, *100*, 229.
(81) Cava, R. J.; Santoro, A.; Murphy, D. W.; Zahurak, S. M.; Fleming, R. M.; Marsch, P.; Roth, R. S. *J. Solid State Chem*. **1986**, *65*, 63.
(82) Broussely, M.; Labat, J.; Bodet, J. M.; Cocciantelli, J. M. *J. Power Sources* **1991**, *13*, 429.
(83) Labat, J.; Cocciantelli, J. M. French Patent 8916337, 1989.
(84) Delmas, C.; Cognac-Auradou, H.; Cocciantelli, J. M.; Ménétrier, M.; Doumerc, J. P. *Solid State Ionics* **1994**, *69*, 257.
(85) Delmas, C.; Brèthes, S.; Ménétrier, M. *J. Power Sources* **1991**, *34*, 113.
(86) Delmas, C. In *Lithium Batteries: New Materials, Developments and Perspectives*; Pistoia, G., Ed.; Elsevier: Amsterdam, 1994; p 457.
(87) Delmas, C. Cognac-Auradou, H.; Cocciantelli, J. M.; Ménétrier, M.; Doumerc, J. P. *Solid State Ionics* **1994**, *69*, 257.
(88) Zakharova, G. S.; Volkov, V. L. *Russ. Chem. Rev.* **2003**, *72*, 311.
(89) Dong, W.; Sakamoto, J. S.; Dunn, B. *Sci. Technol. Adv. Mater*. **2003**, *4*, 3.
(90) Ditte, A. C. *R. Acad. Sci. Park* **1885**, *101*, 698.
(91) Biltz, W. *Ber. Dtsch. Chem. Ges*. **1904**, *37*, 1098.
(92) Wegelin, G. Z. *Chem. Ind. Kolloide* **1912**, *11*, 25.
(93) Ostermann, W. *Wiss. Ind. Hamburg* **1922**, *1*, 17.
(94) Mmer, E. Z. *Chem. Ind. Kolloide* **1911**, *8*, 302.
(95) Gharbi, N.; RKha, C.; Ballutaud, D.; Michaud, M.; Livage, J.; Audiere, J. P.; Schiffmacher, G. *J. Non-Cryst. Solids* **1981**, *46*, 247.
(96) Sanchez, C.; Livage, J.; AudiBre, J. P.; Madi, A. *J. Non-Cryst. Solids* **1984**, *65*, 286
(97) Livage, J. *Coord. Chem. Rev.* **1998**, *178*−*180*, 999.
(98) Le, D. B.; Passerini, S.; Tipton, A. L.; Owens, B. B.; Smyrl, W. H. *J. Electrochem. Soc.* **1995**, *142*, L102.
(99) Harreld, J. H.; Dunn, B.; Nazar, L. F. *Int. J. Inorg. Mater.* **1999**, *1*, 135.
(100) Desai, S. D.; Cussler, E. L. *Langmuir* **1998**, *14*, 277.
(101) Alnoso, B.; Livage, J. *J. Solid State Chem*. **1999**, *148*, 16.
(102) Fontenot, C. J.; Wiench, J. W.; Pruski, M.; Schrader, G. L. *J. Phys. Chem. B* **2000**, *104*, 11622.
(103) Holland, G. P.; Huguenin, F.; Torresi, R. M.; Buttry, D. A. *J. Electrochem. Soc*. **2003**, *150* (6), A721.
(104) Ozin, G. A. *Adv. Mater*. **1992**, *4*, 612.
(105) Engineering a Small World: From Atomic Manipulation to Microfabrication. *Science* **1991**, *254*, 1300 (special section).
(106) Hulteen, J. C.; Martin, C. R. *J. Mater. Chem*. **1997**, *7*, 1075.
(107) Cao, G. Z. *J. Phys. Chem. B* **2004**, *108*, 19921.
(108) Byrappa, K.; Yoshimura, M. *Handbook of Hydrothermal Technology*; Noyes: Park Ridge, NJ, 2001.
(109) Niederberger, M.; Muhr, H. J.; Krumeich, F.; Bieri, F.; Gnther, D.; Nesper, R. *Chem. Mater*. **2000**, *12*, 1995.
(110) Che, G.; Jirage, K. B.; Fisher, E. R.; Martin, C. R. *J. Electrochem. Soc*. **1997**, *144*, 4296.
(111) Sides, C. R.; Li, N.; Patrissi, C. J.; Scrosati, B.; Martin, C. R. *MRS Bull*. **2002**, *27*, 604.
(112) Li, N.; Martin, C. R. *J. Electrochem. Soc*. **2001**, *148*, A164.
(113) Nishizawa, M.; Mukai, K.; Kuwabata, S.; Martin, C. R.; Yoneyama, H. *J. Electrochem. Soc*. **1997**, *144*, 1923.
(114) Patrissi, C. J.; Martin, C. R. *J. Electrochem. Soc*. **1999**, *146*, 3176.

(115) Ratnakumar, B. V.; Smart, M. C.; Huang, C. K.; Perrone, D.; Surampudi, S.; Greenbaum, S. G. *Electrochim. Acta* **2000**, *45*, 1513.
(116) Plichta, E. J.; Hendrickson, M.; Thompson, R.; Au, G.; Behl, W. K.; Smart, M. C.; Ratnakumar, B. V.; Surampudi, S. *J. Power Sources* **2001**, *94*, 160.
(117) Nagasubramanian, G. *J. Appl. Electrochem.* **2001**, *31*, 99.
(118) Lin, H. P.; Chua, D.; Salomon, M.; Shiao, H. C.; Hendrickson, M.; Plichta, E.; Slane, S. *Electrochem. Solid State. Lett.* **2001**, *4*, A71.
(119) Sides, C. R.; Martin, C. R. *Adv. Mater.* **2005**, *17*, 125.
(120) Che, G.; Lakshmi, B. B.; Martin, C. R.; Fisher, E. R.; Ruoff, R. A. *Chem. Mater.* **1998**, *10*, 260.
(121) Che, G.; Fisher, E. R.; Martin, C. R. *Nature* **1998**, *393*, 346.
(122) Che, G.; Lakshmi, B. B.; Martin, C. R.; Fisher, E. R. *Langmuir* **1999**, *15*, 750.
(123) Nishizawa, M.; Mukai, K.; Kuwabata, S.; Martin, C. R.; Yoneyama, H. *J. Electrochem. Soc.* **1997**, *144*, 1923.
(124) Li, N.; Patrissi, C. J.; Martin, C. R. *J. Electrochem. Soc.* **2000**, *147*, 2044.
(125) Patrissi, C. J.; Martin, C. R. *J. Electrochem. Soc.* **1999**, *146*, 3176.
(126) Patrissi C. J.; Martin, C. R. *J. Electrochem. Soc.* **2001**, *148*, A1247.
(127) Li, N.; Martin, C. R.; Scrosati, B. *Electrochem. Solid-State Lett.* **2000**, *3*, 316.
(128) Martin, C. R.; Li, N.; Scrosati, B. *J. Power Sources* **2001**, *97*−*98*, 240.
(129) Li, N.; Martin, C. R. *J. Electrochem. Soc.* **2001**, *148*, A164.
(130) Lakshmi, B. B.; Patrissi, C. J.; Martin, C. R. *Chem. Mater.* **1997**, *9*, 2544.
(131) Cepak, V. M.; Hulteen, J. C.; Che, G.; Jirage, K. B.; Lakshmi, B. B.; Fisher, E. R.; Martin, C. R. *J. Mater. Res.* **1998**, *13*, 3070.
(132) Che, G.; Jirage, K. B.; Fisher, E. R.; Martin, C. R.; Yoneyama, H. *J. Electrochem. Soc.* **1997**, *144*, 4296.
(133) van der Drift, A. *Philips Res. Rep.* **1968**, *22*, 267.
(134) Penn, R. L.; Banfield, J. F. *Geochim. Cosmochim. Acta* **1999**, *63*, 1549.
(135) Chun, C. M.; Navrotsky, A.; Aksay, I. A. *Proc. Microscopy and Microanalysis*; Jones & Begell: New York, 1995; p 188.
(136) Artuso, F.; Bonino, F.; Decker, F.; Lourenco, A.; Masetti, E. *Electrochim. Acta* **2002**, *47*, 2231.
(137) Rauh, R. D. *Electrochim. Acta* **1999**, *44*, 3165.
(138) Ajayan, P. M.; Stephan, O.; Redlich, P.; Colliex, C. *Nature* **1995**, *375*, 564.
(139) Liu, Y. J.; Cowen, J. A.; Kaplan, T. A.; DeGroot, D. C.; Schindler, J.; Kannewurf, C. R.; Kanatzidis, M. G. *Chem. Mater.* **1995**, *7*, 1616.
(140) Lee, K.; Wang, Y.; Cao, G. Z. *J. Phys. Chem. B* **2005**, *109*, 16700.
(141) Nesper, R.; Spahr, M. E.; Niederberger, M.; Bitterli, P. Int. Patent Appl. PCT/CH97/00470, 1997.
(142) Spahr, M. E.; Bitterli, P.; Nesper, R.; Müller, M.; Krumeich, F.; Nissen, H.-U. *Angew. Chem.* **1998**, *110*, 1339.
(143) Spahr, M. E.; Bitterli, P.; Nesper, R.; Müller, M.; Krumeich, F.; Nissen, H.-U. *Angew. Chem., Int. Ed.* **1998**, *37*, 1263.
(144) Krumeich, F.; Muhr, H.-J.; Niederberger, M.; Bieri, F.; Schnyder, B.; Nesper, R. *J. Am. Chem. Soc.* **1999**, *121*, 8324.
(145) Muhr, H.-J.; Krumeich, F.; Schòholzer, U. P.; Bieri, F.; Niederberger, M.; Gauckler, L. J.; Nesper, R. *Adv. Mater.* **2000**, *12*, 231.
(146) Niederberger, M.; Muhr, H.-J.; Krumeich, F.; Bieri, F.; Gnther, D.; Nesper, R. *Chem. Mater.* **2000**, *12*, 1995.
(147) Nesper, R.; Muhr, H.-J.; Niederberger, M. Int. Patent Appl. PCT/CH00/00570, 2000.
(148) Niederberger, M. Dissertation No. 13971, ETH, Zürich, Switzerland, 2000.
(149) Bieri, F.; Krumeich, F.; Muhr, H.-J.; Nesper, R. *Helv. Chim. Acta* **2001**, *84*, 3015.
(150) Wrle, M.; de Onate, J.; Muhr, H.-J.; Bieri, F.; Nesper, R. *Chimia* **1999**, *53*, 336.
(151) Wang, X.; Liu, L.; Bontchev, R.; Jacobson, A. J. *Chem. Commun.* **1998**, 1009.
(152) Pillai, K. S.; Krumeich, F.; Muhr, H.-J.; Niederberger, M.; Nesper, R. *Solid State Ionics* **2001**, *141*−*142*, 185.
(153) Reinoso, J. M.; Muhr, H.-J.; Krumeich, F.; Bieri, F.; Nesper, R. *Helv. Chim. Acta* **2000**, *83*, 1724.
(154) Krumeich, F.; Muhr, H.-J.; Niederberger, M.; Bieri, F.; Reinoso, M.; Nesper, R. *Mater. Res. Soc. Symp. Proc.* **2000**, *581*, 393.
(155) Nordlinder, S.; Edstrom, K.; Gustafsson, T. *Electrochem. Solid-State Lett.* **2001**, *4*, A129.
(156) Dobley, A.; Ngala, K.; Yang, S.; Zavalij, P. Y.; Whittingham, M. S. *Chem. Mater.* **2001**, *13*, 4382.
(157) Krumeich, F.; Muhr, H.-J.; Niederberger, M.; Bieri, F.; Nesper, R. *Z. Anorg. Allg. Chem.* **2000**, *626*, 2208.
(158) Sun, D.; Kwon, C. W.; Baure, G.; Richman, E.; MacLean, J.; Dunn, B.; Tolbert, S. H. *Adv. Funct. Mater.* **2004**, *14*, 1197.
(159) Zhang, T. S.; Hing, P.; Li, Y.; Zhang, J. C. *Sens. Actuators, B* **1999**, *60*, 208.
(160) Pan, Z. W.; Dai, Z. R.; Wang, Z. L. *Science* **2001**, *291*, 1947.
(161) Yang, P. D.; Yan, H. Q.; Mao, S.; Russo, R.; Johnson, J.; Saykally, R.; Morris, N.; Pham, J.; He, R. R.; Choi, H. J. *Adv. Funct. Mater.* **2002**, *12*, 323.
(162) Li, X. L.; Liu, J. F.; Li, Y. D. *Inorg. Chem.* **2003**, *42*, 921.
(163) Wang, X.; Li, Y. D. *J. Am. Chem. Soc.* **2002**, *124*, 2880.
(164) Comini, E.; Faglia, G.; Sberveglieri, G.; Pan, Z. W.; Wang, Z. L. *Appl. Phys. Lett.* **2002**, *81*, 1869.
(165) Law, M.; Kind, H.; Messer, B.; Kim, F.; Yang, P. D. *Angew. Chem., Int. Ed.* **2002**, *41*, 2405.
(166) Pan, D.; Zhang, S.; Chen, Y.; Hou, J. G. *J. Mater. Res.* **2002**, *17*, 1981.
(167) Schlecht, U.; Knez, M.; Duppel, V.; Kienle, L.; Burghard, M. *Appl. Phys. A* **2004**, *78*, 527.
(168) Micocci, G.; Serra, A.; Tepore, A.; Capone, S.; Rella, R.; Siciliano, P. *J. Vac. Sci. Technol. A* **1997**, *15*, 34.
(169) Donnet, J. B. *C. R. Acad. Sci. Paris* **1948**, 508.
(170) Takiyama, K. *Bull. Chem. Soc. Jpn., Int. Ed.* **1958**, *31*, 329.
(171) Kistler, S. S. *J. Phys. Chem.* **1931**, *35*, 815.
(172) Juliusburger, F.; Pirquet, A. *Trans. Faraday Soc.* **1936**, 445.
(173) Errera, J.; Overbeek, J. Th.; Sack, H. *J. Chim. Phys. Phys.-Chim. Biol.* **1935**, *32*, 681.
(174) Donnet, J. B. *J. Chim. Phys. Phys.-Chim. Biol.* **1953**, *50*, 291.
(175) Bailey, J. K.; Nagase, T.; Pozarnsky, G. A.; MeCartney, M. L. Better Ceramics through Chemistry IV. *Mater. Res. Soc. Symp. Proc.* **1990**, *180*, 759.
(176) Livage, J.; Henry, M.; Sanchez, C. *Prog. Solid State Chem.* **1988**, *18*, 259.
(177) Legendre, J. J., Livage, J. *J. Colloid Interface Sci.* **1983**, *94*, 75.
(178) Baughman, R. H. In *Conjugated Polymeric Materials: Opportunities in Electronics, Optoelectronics, and Molecular Electronics*; NATO ASI Series E: Applied Sciences; Bredas, J. L., Chance, R. R., Eds.; Kluwer: Dordrecht, The Netherlands, 1990; Vol. 182, pp 559−582.
(179) Baughman, R. H.; Cui, C.; Zakhidov, A. A.; Iqbal, Z.; Barisci, J. N.; Spinks, G. M.; Wallace, G. G.; Mazzoldi, A.; De Rossi, D.; Rinzler, A. G.; Jaschinski, O.; Roth, S.; Kertesz, M. *Science* **1999**, *284*, 1340.

CM052765H